Research Square

Preprints are preliminary reports that have not undergone peer review.
They should not be considered conclusive, used to inform clinical practice,
or referenced by the media as validated information.

Eosinophil peroxidase promotes the switch from pro-inflammatory to pro-resolving macrophages and ameliorates LPS-induced lung inflammation.

Darja Andreev

darja.andreev@tu-dresden.de

Technische Universität Dresden

Lady Tatiana Albarracin Melo

Friedrich-Alexander-Universität Erlangen Nürnberg and Universitätsklinikum Erlangen

Mohammed Safhi

Friedrich-Alexander-Universität Erlangen Nürnberg and Universitätsklinikum Erlangen

Pauline Porschitz

Technical University Dresden

Md Adnan Karim

Friedrich-Alexander-Universität Erlangen Nürnberg and Universitätsklinikum Erlangen

René Pfeifle

Friedrich-Alexander-Universität Erlangen Nürnberg and Universitätsklinikum Erlangen

Ashwin Rajaseker

Technical University Dresden

Yussuf Hajjaj

Friedrich-Alexander-Universität Erlangen-Nürnberg and Universitätsklinikum Erlangen

Jean-Philippe Auger

Charité – Universitätsmedizin Berlin

Gerhard Kronke

Charité, Berlin Medical School https://orcid.org/0000-0002-7566-4325

Georg Schett

Uniklinikum Erlangen https://orcid.org/0000-0001-8740-9615

Aline Bozec

Department of Internal Medicine 3, Rheumatology and Immunology, Friedrich-Alexander-Universität Erlangen Nürnberg and Universitätsklinikum Erlangen https://orcid.org/0000-0001-8174-2118

Article

Keywords: Eosinophils, Eosinophil peroxidase, Macrophage polarization, Acute lung injury, Resolution of inflammation

Posted Date: November 12th, 2026

DOI: https://doi.org/10.21203/rs.3.rs-11481985/v1

License: This work is licensed under a Creative Commons Attribution 4.0 International License.
Read Full License

Additional Declarations: (Not answered)

Title: Eosinophil peroxidase promotes the switch from pro-inflammatory to pro-resolving macrophages and ameliorates LPS-induced lung inflammation.

Authors

Lady Tatiana Albarracin Melo[1,2#], Mohammed Safhi[1,2#], Pauline Porschitz[3], Md Adnan Karim[1,2], René Pfeifle[1,2], Ashwin Rajaseker[3], Yussuf Hajjaj[4], Jean-Philippe Auger[1,2,5,6], Gerhard Krönke[1,2,5,6], Georg Schett[1,2], Aline Bozec[1,2†*], Darja Andreev[3†*]

# These authors contributed equally to this work

† These authors jointly supervised this work

* Corresponding author

Affiliations

[1] Department of Internal Medicine 3, Rheumatology and Immunology, Friedrich-Alexander-Universität Erlangen Nürnberg and Universitätsklinikum Erlangen; Erlangen, Germany.

[2] Deutsches Zentrum Immuntherapie, Friedrich-Alexander-Universität Erlangen Nürnberg and Universitätsklinikum Erlangen; Erlangen, Germany.

[3] Center for Regenerative Therapies Dresden (CRTD), Technical University (TU) Dresden; Dresden, Germany.

[4] Department of Experimental Medicine 1, Friedrich-Alexander-Universität Erlangen-Nürnberg and Universitätsklinikum Erlangen; Erlangen, Germany.

[5] Department of Rheumatology and Clinical Immunology, Charité – Universitätsmedizin Berlin; Berlin, Germany.

[6] Deutsches Rheuma-Forschungszentrum Berlin; Berlin, Germany.

Correspondence:

Darja Andreev:

Center for Regenerative Therapies Dresden (CRTD)

Fetscherstr. 105, 01307 Dresden, Germany

+49 (0)351 458 82004

Darja.andreev@tu-dresden.de

Aline Bozec:

Nikolaus-Fiebiger-Zentrum (NFZ)

Glückstr. 6, 91054 Erlangen, Germany

+49 (0)9131 85 33717

Aline.bozec@uk-erlangen.de

Key words

Eosinophils; Eosinophil peroxidase, Macrophage polarization; Acute lung injury, Resolution of inflammation

Abstract

Eosinophils are traditionally recognized as immune effector cells in allergic and parasitic diseases, but their emerging roles in tissue homeostasis make them particularly intriguing cells to study in the context of tissue inflammation. Our study uncovers a previously unrecognized crosstalk between eosinophils and macrophages that is essential for resolving inflammation. Single-cell RNA sequencing shows that eosinophil deficiency leads to a global hyperactivated monocyte/macrophage lineage, underscoring the baseline regulatory role of eosinophils in myeloid homeostasis. We identify eosinophil peroxidase (EPX), a protein long associated with cytotoxicity and tissue damage, as the key mediator of macrophage regulation by eosinophils. We demonstrate that EPX orchestrates a time-dependent reprogramming of macrophages, driving a transition from a pro-inflammatory to a pro-resolving phenotype. This shift is characterized by metabolic flexibility, transient mitochondrial activation followed by redox homeostasis, and enhanced efferocytosis. This EPX-driven macrophage shift dependents on CD11b signaling. Notably, systemic or intranasal EPX administration attenuates LPS-induced acute lung injury, preserving alveolar macrophages and promoting a regulatory interstitial macrophage signature. Our findings reveal a previously unrecognized EPX-CD11b-metabolic axis that drives macrophage-mediated resolution of inflammation.

Introduction

Eosinophils have long been regarded as the hallmark effector cells of type-2 immunity, best known for their roles in host defense against helminths and in the pathogenesis of allergic diseases such as asthma and atopic dermatitis (1). Their granules contain a repertoire of cationic proteins—major basic protein, eosinophil-derived neurotoxin, eosinophil cationic protein, and eosinophil peroxidase (EPX)—that are released upon degranulation and can exert acute cytotoxic and pro-inflammatory effects (2). Emerging evidence, however, suggests that eosinophil-derived mediators can also act in a regulatory capacity, shaping the phenotype and function of neighboring immune cells (3, 4). In particular, the interaction between eosinophils and macrophages has attracted growing interest.

Macrophages play a central and highly dynamic role in the initiation, progression, and resolution of both acute and chronic inflammatory diseases. Their functions can be both protective and pathogenic, depending on their activation state, tissue environment, and disease context. Macrophages originate either from blood-born monocytes homing to tissue or are placed there in early development as tissue-resident macrophages, which can locally maintain themselves through self-renewal (5). Macrophage phenotype is largely shaped by local microenvironmental cues, which establish tissue-specific regulatory signatures (6).

During inflammation, monocyte-derived macrophages exhibit remarkable plasticity. In response to pathogen-associated molecular patterns (PAMPs), danger-associated molecular patterns (DAMPs), or pro-inflammatory cytokines like IFN-γ, macrophages undergo metabolic and epigenetic reprogramming to adopt a classically activated phenotype (CAMs) (7). These cells express high levels of inducible nitric oxide synthase (iNOS) and secrete pro-inflammatory mediators such as TNFα, IL-1β, and IL-6, playing a central role in pathogen clearance and early immune defense (8). While this response is crucial for host protection, sustained pro-inflammatory macrophage polarization contributes to tissue damage and chronic inflammation. In acute-lung injury (ALI), overactivation of macrophages leads to excessive cytokine production, increased vascular permeability, and impaired gas exchange (9).

Notably, resolution of inflammation depends on a transition from a pro-inflammatory to a pro-resolving macrophage phenotype, referred to as alternatively activated macrophages (AAMs). These cells are commonly induced by IL-4 and IL-13 through the STAT6 signaling pathway and express characteristic markers such as arginase-1 (ARG1), resistin-like molecule-alpha (RELMα), and Chitinase-like 3 (Chi3l3) (8). Interestingly, their polarization can also be promoted by inflammation-associated mediators like IL-33 (10). AAMs facilitate resolution of inflammation by secreting regulatory cytokines like IL-10 and TGF-β, and by clearing apoptotic cells, particularly neutrophils, through efferocytosis (11). In the context of ALI, their timely appearance is associated with restoration of lung integrity and barrier function (9). The functional plasticity of macrophages is tightly coupled to metabolic reprogramming: classical macrophages rely predominantly on aerobic glycolysis, whereas AAMs depend on oxidative phosphorylation (OXPHOS) and fatty-acid oxidation to sustain their reparative programs (12).

The notion that eosinophils can influence macrophage polarization is supported by several recent studies. For instance, eosinophils are required for the maintenance of AAMs in adipose tissue and thereby contribute to glucose tolerance (13). In zymosan-induced inflammation, eosinophil depletion leads to the breakdown of the AAM-enriched anti-inflammatory region, accompanied by decreased efferocytosis and increased neutrophil recruitment (14). Using an inflammatory arthritis model, we previously demonstrated that eosinophils exert a pro-resolving effect in the synovium by driving macrophages toward an AAM phenotype (15, 16). Notably, eosinophils are key mediators of tissue repair following injury, in part by modulating macrophage activity (17). However, the specific molecular mediators responsible for this bidirectional communication remain incompletely defined. Among the granule proteins, EPX is uniquely positioned to act as a redox-active signaling molecule: it catalyzes the formation of hypobromous acid (HOBr) and other reactive oxidants that can modify proteins, lipids, and nucleic acids (18). While such oxidative modifications are often associated with tissue damage, they can also serve as signaling cues that modulate receptor activity and downstream transcriptional programs (19). Indeed, EPX has been shown to influence dendritic-cell activation and to alter neutrophil chemotaxis, hinting at a broader immunomodulatory repertoire (20, 21). Despite these intriguing observations, the direct impact of EPX on macrophage polarization and metabolism has not been fully investigated.

In this study, we therefore set out to define the role of eosinophils and specifically EPX in modulating macrophage plasticity during inflammation. Using single-cell RNA sequencing, we revealed that eosinophil deficiency reshapes the monocyte/macrophage compartment in both bone-marrow and peritoneal niches. Moreover, we demonstrated that EPX reprograms macrophages from a pro-inflammatory toward a regulatory, metabolically active state, and that CD11b is a critical conduit for EPX-mediated effects. Notably, EPX administration attenuated LPS-driven lung injury, reduced pro-inflammatory cytokine levels, and promoted a favorable shift in the composition of macrophages within the lung tissue. Collectively, our findings identify a previously unappreciated role for EPX in modulating macrophage responses during the transition from inflammation to resolution, revealing a context-dependent function of EPX that extends beyond its established pro-inflammatory and cytotoxic activities.

Materials and methods

Study Design

The sample sizes used in the experiments followed common practice in the field and were confirmed using G*Power (version 3.1.9.7). Mice were randomly assigned to the experimental groups, which were distributed across cages to minimize potential cage-related confounding factors. For all experiments, all samples that met the predefined quality control criteria (e.g., correct genotype, successful disease induction, adequate staining quality, and reliable gene expression measurements) were included in the statistical analyses. These exclusion criteria were established prior to data collection. All experimental findings were independently reproduced in at least three experiments, and representative results are shown.

Mouse experiments

Mice

Wild-type BALB/cJRj mice were obtained from Janvier Labs. ΔdblGATA mice (eosinophil-deficient)(22) were maintained on a BALB/c background, and Cx3cr1-Cre R26-tdTomato reporter mice(23) were on a C57BL/6 background. Steady-state analyses were performed on nine- to eleven-week-old animals of both sexes. All mice were housed in a specific-pathogen-free (SPF) facility at 22–23 °C, 50–60 % relative humidity, with a 12-h light/dark cycle and ad libitum access to standard chow (ssniff, V1534-000) and water. Euthanasia was carried out by gradual CO_2 inhalation. All procedures complied with the regulations of the Franz-Penzoldt-Zentrum (FPZ) animal facility in Erlangen and were approved by the ethics committees of the government of Unterfranken (Regierung von Unterfranken, Germany).

LPS-induced lung injury

In the LPS-induced lung-injury experiment, nine-week-old BALB/cJRj mice were administered 40 µg LPS (Mdbioproducts; Cat# MDLPS5-0) intranasally (i.n.) on day 0. On the same day they received either an intravenous (i.v.) injection of 40 µg eosinophil peroxidase (EPX; Abbexa; Cat# Abx653285) or an intranasal (i.n.) challenge with 10 µg EPX. Mice were kept under standard housing conditions for three days. A subset of animals was sacrificed on day 1 to assess early responses. The remaining groups received a second i.v. dose of 40 µg EPX or an i.n. dose of 10 µg EPX on day 2, and were euthanized by CO_2 inhalation on day 3.

Histology of lung tissue

For histological analysis, a portion of the lung tissue was fixed overnight in 4% paraformaldehyde (PFA) in PBS (pH 7.4) and subsequently transferred to 70% ethanol. The tissue was paraffin-embedded, and serial 2-µm sections were prepared and stained with hematoxylin and eosin (H&E) according to standard protocols. Images were acquired using a Keyence BZ-X710 microscope with the BZ-X View and BZ-X Analyzer software (version 2.22; Keyence) at x10 magnification using a Nikon PlanApo λ 10×/0.45, 4 mm objective. The resulting images were used for lung injury scoring.

Immunofluorescence of lung tissue

Freshly isolated lung tissues were embedded in OCT Compound (Sakura Finetek; Thermo Fisher Scientific, Cat# 12351753) and rapidly frozen. Cryosections (7 µm) were cut using a Leica CM3050 S cryostat (Leica Biosystems). Sections were air-dried for 15 min, fixed in 4%

PFA for 10 min at room temperature (RT), rinsed with distilled water, and washed in TBS-T. Sections were blocked with TBS-T containing 5% bovine serum albumin (BSA; Merck, Cat# A8806) for 1 h at RT and subsequently washed in TBS-T. The Primary antibodies anti-mouse CD86 Alexa Fluor 700 (clone A17199, 1:100; BioLegend, Cat# 159214) and anti-mouse CD273 (PD-L2) PE (clone TY25, 1:100; BioLegend, Cat# 107205) were diluted in 5% BSA/TBS-T and incubated overnight at 4°C in a humidified chamber. The next day, sections were washed in TBS-T, then TBS, and briefly rinsed with distilled water. Slides were mounted with DAPI-containing antifade mounting medium (Vector Laboratories, Cat# H-1200-10), cover slipped carefully to avoid air bubbles, and stored at 4°C until imaging. Images were acquired using a Keyence BZ-X710 microscope with BZ-X View and BZ-X Analyzer software (v2.22) at x20 magnification. Fluorescence signal quantification was performed using Fiji (ImageJ).

Single cell isolation

For bone marrow extraction, femurs and tibias were dissected, cleared of surrounding tissue, and flushed with ice-cold 1xPBS (Thermo Fisher Scientific; Cat# 15326239). The cell suspension was dissociated by gentle pipetting, filtered through a 70 µm cell strainer, and treated with red blood cell (RBC) lysis buffer. After washing and centrifugation, cells were resuspended and counted for subsequent analyses.

Peritoneal lavage was performed with 10 mL ice-cold PBS using a 25-G needle. After gently massaging the abdomen for 1–2 minutes, the fluid was aspirated, filtered through a 70 µm strainer, washed, centrifuged, and the resulting cell pellet was resuspended and counted for downstream analyses.

Lungs were harvested into 5 mL ice-cold PBS, minced in a sterile Petri dish with scalpels, and transferred to 5 mL RPMI (Thermo Fisher Scientific; Cat# 61870036) supplemented with 10 % FBS (Merck; Cat# 12103C), 1 % PenStrep (Merck; Cat# P0781), 1 mg/mL collagenase A (Merck; Cat#10103578001), and 0.1 mg/mL DNase I (Merck; Cat# 11284932001). The mixture was incubated at 37 °C for 45 min with gentle shaking, then passed through a 40 µm strainer. After red-blood-cell lysis, the cells were washed, centrifuged, resuspended, and counted for downstream analyses.

Spectral flow cytometry

For surface marker staining, isolated single cells were incubated with Zombie NIR (1:1000; Biolegend; Cat# 423106) and the antibodies listed in table 1 diluted in 1x PBS in the dark at 4 °C for 20 min.

Table 1: Antibodies for spectral flow cytometry.

Antibody	Fluorophore	Dilution	Company	Clone	Cat#
Anti-mouse CD45	BV785	1:400	Biolegend	30-F11	103149
Anti-mouse/human CD11b	Spark Blue 550	1:400	Biolegend	M1/70	101290
Anti-mouse Ly6G	PerCP/Cy5.5	1:400	Biolegend	1A8	127616
Anti-mouse Ly6C	APC/Fire 810	1:400	Biolegend	Hk1	128056

Anti-mouse F4/80	PE-Cy5	1:400	Biolegend	BM8	123112
Anti-mouse Siglec-F	BV421	1:400	Biolegend	S17007L	155509
Anti-mouse CD11c	PE/Dazzle 594	1:400	Biolegend	N418	117348
Anti-mouse MERTK (Mer)	APC	1:200	Biolegend	2B10C42	151508
Anti-mouse CD206 (MMR)	BV650	1:200	Biolegend	C068C2	141723
Anti-mouse I-A/I-E	APC-Cy7	1:400	Biolegend	M5/114.15.2	107628

After washing, cells were resuspended in FACS buffer (1x PBS with 2% FBS and 2 mM EDTA) for spectral flow cytometric analyses using the Cytek Northern Lights spectral flow cytometer (Cytek Biosciences). Spectral unmixing was conducted using SpectroFlo software (Cytek Biosciences) based on single-stained controls. Data were analyzed by FlowJo (BD Biosciences).

Single cell RNA sequencing

Single cells were isolated from the bone marrow and peritoneum of 9–11-week-old male wild-type Balb/c and ΔdblGATA mice. Five mice were pooled per experimental group. Cells were stained with anti-CD45 APC-eFluor™ 780 antibody (clone 30-F11; 1:800; eBioscience; Cat# 47-0451-82) in 1× PBS for 20 minutes in the dark at 4 °C. Following staining, cells were washed and resuspended in FACS buffer. CD45+ cells were then sorted using the MoFlo Astrios EQ flow cytometer at the Core Unit Cell Sorting and Immunomonitoring facility, Friedrich-Alexander-Universität Erlangen-Nürnberg.

Single-cell RNA sequencing (scRNA-seq) was carried out at the NGS Core Unit, Friedrich-Alexander-Universität Erlangen-Nürnberg. Sorted CD45+ cells were washed and prepared according to the Chromium Next GEM Single Cell 3' Reagent Kit v3.1 protocol. During cDNA library construction, cDNA concentration was quantified using a Qubit fluorometer, and two quality control assessments were performed using a Bioanalyzer. The resulting libraries were stored at –20 °C until further processing. Sequencing was performed on a NovaSeq 6000 platform using a paired-end 150 (PE150) configuration, with a target depth of 50,000 read pairs per cell. Post-sequencing, data quality was evaluated. Raw fastq files were generated by the NGS Core Unit. All original scRNA-seq data (fastq files) have been deposited in the Gene Expression Omnibus (GEO) database under the accession code GSE348040 and GSE347683.

Fastq files were processed using Cellranger (v9.0.1) for alignment to the mouse reference genome (mm10-2020/GRCm38) and gene expression quantification, and the resulting filtered feature-barcode matrices were analyzed downstream in R (v4.4.0) using Seurat (v5.2.1).Cells with 500–6,500 detected genes, 1,000–50,000 unique molecular identifiers (UMIs), and less than 8% mitochondrial reads were retained for downstream analysis. Gene expression data were log-normalized, and the 2,000 most highly variable genes were selected for principal component analysis (50 components). Clustering was performed on the first 25 principal components using the Louvain algorithm (resolution = 0.3), and results were visualized by uniform manifold approximation and projection (UMAP). Cell-type identities were initially predicted using CellTypist with the Immune_all_low model, followed by manual refinement of granulocyte and macrophage subtype annotations, and cluster-level identities were assigned by majority-vote consensus, applied to all cells within each cluster. Differential expression

between genotypes (wild-type vs. ΔdblGATA) and cell populations was assessed using the Wilcoxon rank-sum test (Seurat FindMarkers; adjusted $p < 0.05$, $|log2FC| > 0.25$), visualized using ggplot2 (v3.5.1) and ggrepel (v0.9.6). Functional enrichment was performed using clusterProfiler (v4.14.6), including KEGG over-representation and gene set enrichment analysis (GSEA), with mouse gene annotations via org.Mm.eg.db (v3.20.0) and visualization via enrichplot (v1.26.6). Transcription factor activity was inferred using the univariate linear model (ULM) in decoupleR (v2.12.0) against the dorothea mouse regulon (v1.18.0), restricted to high-confidence (A/B/C) interactions.

Enzyme-linked immunosorbent assay (ELISA)

Blood was collected in BD Microtainer® blood collection tubes and serum was isolated by centrifugation. Serum levels of TNFα, IFN-γ, and IL-6 were measured by ELISA using mouse TNF-alpha (R&D Systems; Cat# DY410), mouse IFN-gamma (R&D Systems; Cat# DY485), and mouse IL-6 (R&D Systems; Cat# DY406) DuoSet ELISA Kit according to the manufacturer's instructions. The optical density was measured at 450 nm with a wavelength correction at 540 nm using the SpectraMax190 system with the SoftMax Pro v.7.1 software (Molecular Devices).

Primary macrophage culture

Bone marrow-derived macrophages (BMDMs)

Bone marrow cells were isolated from the femurs and tibias of 9- to 11-week-old BALB/cJRj or Cx3cr1 Cre R26 tdTomato reporter mice. Cells were cultured at 37 °C in a 5% CO_2 incubator in BMDM differentiation medium composed of Dulbecco's Modified Eagle Medium (DMEM; Thermo Fisher Scientific; #11960044) supplemented with 10% fetal calf serum (FCS; Thermo Fisher Scientific; Cat# A5256701), 1% penicillin–streptomycin (Thermo Fisher Scientific; Cat# 15140122), 1% L-glutamine (Thermo Fisher Scientific; Cat# 25030024), 1% non-essential amino acids (NEAA; Thermo Fisher Scientific; Cat# 11140035), and 20% M-CSF-containing L929 cell-conditioned supernatant. On the day following isolation, 0.5×10^6 non-adherent cells per mL were seeded into fresh BMDM differentiation medium and cultured for 7 days, with medium replenished on day 3.

After 7 days of culture, BMDMs were detached using CellStripper (Thermo Fisher Scientific; Cat# 15313661). Successful differentiation was confirmed by flow cytometry using the following antibodies: anti-CD45 APC-eFluor™ 780 (clone 30-F11; 1:800; eBioscience; Cat# 47-0451-82), anti-CD11b FITC (clone M1/70; 1:400; BD; Cat# 561688), and anti-F4/80 APC (clone BM8; 1:400; BioLegend; Cat# 123116). Subsequently, 0.5×10^6 cells per mL were reseeded into BMDM culture medium consisting of RPMI medium (Thermo Fisher Scientific; Cat# 31870074), 10% FCS, 1% penicillin–streptomycin, and 1% L-glutamine. Cells were incubated overnight at 37 °C in a 5% CO_2 humidified incubator to facilitate detachment and allow for recovery before proceeding with subsequent experiments.

The following day, BMDMs were stimulated under various conditions for 4, 8, or 24 hours, depending on the experimental design, relative to untreated controls. Stimuli included EPX (0.1 µg/mL; Abbexa; Cat# Abx653285), LPS (1 µg/mL; Thermo Fisher Scientific; Cat# 00-4976-93) with or without IFN-γ (0.1 µg/mL; Thermo Fisher Scientific; Cat# 315-05-100UG), and with or without EPX, as well as IL-4 (0.1 µg/mL; Thermo Fisher Scientific; Cat# 214-14-50UG). In selected experiments, cells were pre-incubated with a neutralizing anti-CD11b

antibody (5 µg/mL; BioXCell; Cat# BE0428) or an equivalent concentration of Rat IgG2b isotype control (5 µg/mL; BioXCell; Cat# BE0090) for 1 hour prior to stimulation.

Flow cytometry

To assess the polarization status of BMDMs 24 hours after stimulation, cells were detached using CellStripper and subsequently stained in the dark at 4 °C for 20 min with the antibodies listed in table 2 diluted in 1X PBS.

Table 2: Antibodies for flow cytometry.

Antibody	Fluorophore	Dilution	Company	Clone	Cat#
Anti-mouse CD45	APC-efluor 780	1:800	eBioscience	30-F11	47045182
Rat Anti-CD11b	FITC	1:400	BD	M1/70	561688
Anti-mouse F4/80	APC	1:400	Biolegend	BM8	123116
Anti-mouse F4/80	PE/Cy5	1:400	Biolegend	BM8	123112
Anti-mouse CD86	BV510	1:400	Biolegend	GL1	105040
Anti-mouse I-A/I-E	Pacific blue	1:800	Biolegend	M5/114.15.2	107620
Anti-mouse CD273 (PD-L2)	PE	1:800	Biolegend	TY25	107205
Anti-mouse CD206 (MMR)	BV650	1:400	Biolegend	C068C2	141723
Anti-mouse CD36	PE	1:800	Biolegend	HM36	102606
Anti-mouse CD93	PE/Cy7	1:800	Biolegend	AA4.1	136506
Human/Mouse TREM2	APC	1:400	R&D	237920	FAB17291A

After washing, BMDMs were resuspended in FACS buffer for flow cytometric analyses using the Cytoflex S flow cytometer (Beckman Coulter). Flow cytometry data were analyzed by FlowJo (BD Biosciences). Compensation was performed with single-stained controls.

Real-time qPCR

RNA from BMDMs was extracted using RNA-Solv Reagent (Omega Bio-tek; Cat# R6830-02) according to the manufacturer's instructions. RNA was freed from genomic DNA using DNase I kit (Thermo Fisher Scientific; Cat# EN0521) and reversely transcribed into cDNA using high capacity cDNA Reverse Transcription Kit (Thermo Fisher Scientific; Cat# 4368814). Real-time qPCR was performed using SYBR™ Select Master Mix (Thermo Fisher Scientific; Cat# 44-729-19) on QuantStudio 6 Flex Real-Time PCR System (AppliedBiosystems) with the primers listed in Table 3. Gene expression was normalized with *Actb*.

Table 3: RT-qPCR primers.

Gene	Forward	Reverse
Actb	5′TGTCCACCTTCCAGCAGATGT3′	5′AGCTCAGTAACAGTCCGCCTAGA3′
Acod1	5′TCACAGCTCTATCGGAAGCC3′	5′GGAGGGTGGAATCTCTTTGGT3′

Il10	5′GCTGGACAACATACTGCTAACC3′	5′ATTTCCGATAAGGCTTGGCAA3′
Il1b	5′CAGGCAGGCAGTATCACTCA3′	5′AGGTGCTCATGTCCTCATCC3′
Nos2	5′GTGACCATGGAGCATCCCAA3′	5′TCGAACTCCAATCTCGGTGC3′

Immunofluorescence of BMDMs

For immunofluorescence imaging, BMDMs were cultured in µ-Slide 8 Well high glass-bottom chambers (Ibidi, Cat# 80801). After stimulation for 24 hours with LPS, IL-4, EPX, or control condition, cells were washed with 1x PBS and fixed with 4% PFA for 10 min at RT. Following fixation, cells were washed and blocked with 5% bovine serum albumin (BSA; Merck; Cat# A8806) in 1x PBS for 30 min at RT to minimize non-specific antibody binding. Cells were then incubated for 1 hour at 4 °C with the following fluorescently labeled primary antibodies, diluted in 5% BSA in 1x PBS: anti-mouse CD86 Alexa Fluor 700 (clone A17199; 1:100; BioLegend; Cat# 159214), anti-mouse CD206 Alexa Fluor 594 (clone C068C2; 1:100; BioLegend; Cat# 141726), and anti-mouse CD68 Alexa Fluor 488 (clone M5/114.15.2; 1:100; BioLegend; Cat# 107620). After staining, cells were washed thoroughly and mounted with a fluorescence mounting medium containing DAPI (Vector Laboratories; Cat# H-1200-10) for nuclear counterstaining. Images were acquired using a Keyence BZ-X710 microscope equipped with BZ-X View and BZ-X Analyzer software (version 2.22; Keyence) at x20 magnification. Quantification of fluorescence signals was performed using Fiji (ImageJ) software.

Cytokine assessment in BMDM supernatant

BMDMs were reseeded at a density of 0.5 × 10^6 cells/mL in BMDM culture medium and stimulated under various conditions for 24 hours. After stimulation, supernatants were collected, rapidly frozen in liquid nitrogen, and stored at −80°C until further analysis. Cytokine levels were measured either by ELISA as described or by LEGENDplex™ multiplex immunoassay (BioLegend) using flow cytometry, following the manufacturer's instructions. Analyses were performed using either a Cytoflex S flow cytometer (Beckman Coulter) or a BD LSR Fortessa. Cytokine concentrations were quantified using LEGENDplex™ Data Analysis Software.

Bulk RNA sequencing

Eight and 24 hours after stimulation with LPS, IL-4, EPX, or control condition, total RNA was extracted from BMDMs using RNA-Solv Reagent (Omega Bio-tek; Cat# R6830-02) following the manufacturer's protocol. Bulk RNA sequencing (RNA-seq) was performed by Novogene (Munich). A total amount of 1 µg RNA per sample was used as input material for the RNA sample preparations. Libraries were prepared using poly(A) enrichment and sequenced on an Illumina NovaSeq 6000 platform to generate 150 bp paired-end reads. Novogene performed adapter trimming and quality filtering to remove low-quality reads and adapter sequences. The resulting high-quality clean reads were delivered for downstream bioinformatics analysis. All original RNA-seq data (fastq files) have been deposited in the Gene Expression Omnibus (GEO) database under the accession code GSE347419.

To ensure sequencing quality, we first assessed the raw data using FastQC (v0.11.9). Reads were then aligned to the Mus musculus reference genome (GRCm38/mm10) using the STAR aligner (v2.7.9a) with default parameters. Aligned BAM files were sorted and indexed using SAMtools (v1.11). Gene-level read counts were generated with featureCounts (v2.0.1) using

the M25 mouse gene annotation from GENCODE. Differential gene expression analysis was conducted using DESeq2 (v1.46.0) in R (v4.4.0). Genes were considered significantly differentially expressed if they met the following criteria: adjusted *p*-value < 0.05 (Benjamini-Hochberg correction) and absolute $\log_2$ fold change > 1. Visualization of results was performed using the R packages ggplot2 (v3.5.1), EnhancedVolcano (v1.28.2), and pheatmap (v1.0.12), for generating principal component analyses (PCA), volcano plots, and heatmaps, respectively. Functional enrichment analysis was carried out using clusterProfiler (v4.14.6), including Gene Ontology (GO) term enrichment and KEGG pathway analysis, using KEGG Legacy gene sets obtained via msigdbr (v26.1.0) for Mus musculus, with Ensembl-to-Entrez ID mapping via org.Mm.eg.db (v3.20.0) and enrichment visualization via enrichplot (v1.26.6) to identify biologically relevant processes and pathways associated with the differentially expressed genes. To highlight macrophage- and inflammation-relevant biology specifically, GO Biological Process results were further filtered to terms whose descriptions matched a curated keyword list (macrophage, monocyte, myeloid, phagocytosis, lipopolysaccharide, inflammation, cytokine production, toll-like receptor, innate immune, antigen presentation) where indicated.

Extracellular flux assays using the Seahorse platform (Agilent)

For metabolic analyses, 2 × 10^5 BMDMs in 180 µL of culture medium were seeded onto Seahorse XF96 Cell Culture Microplates (Agilent Technologies; Cat# 103775-100) and stimulated with LPS, IL-4, EPX, or kept in control condition for 24 hours. For the Glycolysis Stress Test, Seahorse XF RPMI Medium (Agilent Technologies; Cat# 103576-100) was supplemented with 2 mM L-glutamine (Agilent Technologies; Cat# 103579-100). For the Mitochondrial Stress Test, the medium was supplemented with 10 mM glucose (Agilent Technologies; Cat# 103577-100), 1 mM pyruvate (Agilent Technologies; Cat# 103578-100), and 2 mM L-glutamine. After stimulation, cells were resuspended in Glyco Assay Medium (for glycolysis) or Mito Assay Medium (for mitochondrial function). Extracellular acidification rate (ECAR) and oxygen consumption rate (OCR) were measured using the Seahorse XF96 Extracellular Flux Analyzer (Agilent Technologies) according to the manufacturer's protocol. For ECAR measurements, the following final concentrations were injected: 10 mM glucose (Merck; Cat# G8270), 2 µM oligomycin (Merck; Cat# 75351), and 50 mM 2-deoxy-D-glucose (Merck; Cat# D8375). For OCR measurements, the following were injected: 2 µM oligomycin, 2 µM carbonyl cyanide 4-(trifluoromethoxy)phenylhydrazone (FCCP; Merck; Cat# C2920), 1 µM rotenone (Merck; Cat# R8875), and 1 µM antimycin A (Merck; Cat# A8674). Data were collected using Seahorse Wave Desktop Software (Agilent Technologies). Changes in ECAR and OCR in response to sequential compound injections were analyzed to calculate key parameters of glycolytic function and mitochondrial respiration, including glycolytic capacity, glycolytic reserve, basal and maximal respiration, ATP-linked respiration, proton leak, and spare respiratory capacity. These calculations were performed using Microsoft Excel.

Mitochondrial ROS and mitochondrial mass measurement

Four or 24 hours after stimulation with LPS, IL-4, EPX, or control condition, BMDMs were washed and stained with either 5 µM MitoSOX™ Red (Thermo Fisher Scientific; Cat# M36008) in HBSS (Thermo Fisher Scientific; Cat# 11570616) for 30 min at 37 °C to assess mitochondrial reactive oxygen species (ROS) levels, or with 10 nM MitoTracker™ Green FM (Thermo Fisher Scientific; Cat# M7514) in HBSS for 30 min at 37 °C to evaluate mitochondrial

mass. Following staining, cells were washed to remove excess dye and then counterstained with 1 µg/mL Hoechst (Thermo Fisher Scientific; Cat# 62249) for 10 min at RT in the dark to label nuclei. Fluorescence imaging was carried out using a Keyence BZ-X710 microscope equipped with BZ-X View and BZ-X Analyzer software (version 2.22; Keyence) at x20 magnification. Fluorescence was quantified using Fiji (ImageJ) software. Quantification included background subtraction and normalization to Hoechst-stained nuclear signals.

Efferocytosis analysis by flow cytometry and live-cell imaging

Twenty-four hours after stimulation with LPS, IL-4, EPX, or control, BALB/cJRj BMDMs plated in standard wells or Cx3cr1 Cre R26 tdTomato BMDMs plated in µ-Slide 8 Well high glass-bottom chambers (Ibidi, Cat# 80801) were incubated for 3 hours with fluorescence-labeled apoptotic neutrophils. Neutrophils were isolated from BALB/cJRj mice using MACS negative selection (Milteny Biotec; Cat# 130-097-658) per manufacturer's instructions. Apoptosis was induced by incubating neutrophils with Staurosporine Apoptosis Inducer (Cayman Chemical; Cat# 601770) for 6 hours at 37°C in a 5% CO_2 incubator, following the efferocytosis assay kit protocol. Apoptotic neutrophils were labeled with pHrodo™ Red (Thermo Fisher Scientific; Cat# P35372) for flow cytometry or CFSE (Cayman Chemical; Cat# 601770) for live-cell imaging, according to the respective manufacturer's protocols.

For flow cytometry, BALB/cJRj BMDMs were additionally stained with anti-CD45 APC-eFluor™ 780 (clone 30-F11; 1:800; eBioscience; Cat# 47-0451-82), anti-CD11b FITC (clone M1/70; 1:400; BD; Cat# 561688), and anti-F4/80 APC (clone BM8; 1:400; BioLegend; Cat# 123116). pHrodo$^+$ BMDMs were analyzed using a Cytoflex S flow cytometer (Beckman Coulter), and data were processed with FlowJo (BD Biosciences). Compensation was performed using single-stained controls.

For live-cell imaging, interactions between CFSE-labeled apoptotic neutrophils and Cx3cr1 tdTomato-positive BMDMs were monitored in RPMI phenol red–free medium (Thermo Fisher Scientific; Cat# 10363083) over 24 hours using a Zeiss Spinning Disc Axio Observer Z1 microscope at 63x magnification, maintained at 37 °C and 5% CO_2 at the Optical Imaging Competence Center (OICE), Friedrich-Alexander-Universität Erlangen-Nürnberg. Images were processed using Imaris software (Oxford Instruments).

Co-localization of CD11b with EPX

BMDMs were seeded at a density of 1.5×10^5 cells per well in µ-Slide 8 Well high glass-bottom chambers (Ibidi, Cat# 80801) and stimulated with EPX for 24 hours, compared to control conditions. EPX was pre-labeled with Atto 647N (red; Merck, Cat# 18373) by incubation for 40 min at room temperature prior to application. After stimulation, cells were processed for immunofluorescence as described. Cells were incubated for 1 hour at 4 °C with anti-CD11b Alexa Fluor 488 (clone M1/70; 1:100; BioLegend, Cat# 101217), washed thoroughly, and mounted with DAPI-containing fluorescence mounting medium (Vector Laboratories, Cat# H-1200-10) for nuclear staining. Images were acquired using a Leica Stellaris 8 confocal microscope with a 63x oil-immersion objective at the Optical Imaging Competence Center (OICE), Friedrich-Alexander-Universität Erlangen-Nürnberg, enabling high-resolution subcellular imaging. Z-stack acquisition was performed to confirm colocalization of Atto 647N-labeled EPX with CD11b. Image analysis and 3D reconstruction were carried out using Imaris software (Oxford Instruments).

Proximity Ligation Assay (PLA) for detection of CD11b–EPX interaction

To assess molecular proximity and potential interaction between CD11b and EPX in BMDMs, a Duolink® In Situ Proximity Ligation Assay (PLA; Merck, Cat# DUO92101) was performed according to the manufacturer's instructions. BMDMs were seeded in µ-Slide 8 Well high glass-bottom chambers (Ibidi, Cat# 80801) and cultured under standard conditions. After 24 hours of stimulation with EPX or vehicle control, cells were washed twice with PBS and fixed with 4% PFA in PBS for 10 min at RT. Fixed samples were rinsed three times with PBS (5 min each) and permeabilized with 0.1% Triton X-100 in PBS for 10 min RT, followed by three additional PBS washes (5 min each). The primary antibodies rabbit anti-EPX (1:100; Biozol; Cat# orb382913) and mouse anti-CD11b (1:100; Biorbyt; Cat# orb651341) were applied and incubated overnight at 4°C. Following the PLA procedure, cells were mounted with fluorescence mounting medium containing DAPI (Vector Laboratories, Cat# H-1200-10) and covered with a coverslip. Fluorescence images were acquired using a Keyence BZ-X710 microscope equipped with BZ-X View and BZ-X Analyzer software (v2.22; Keyence) at x20 magnification. Negative controls were included in all experiments by omitting one or both primary antibodies to assess non-specific background signal. PLA signals were quantified using ImageJ (Fiji) by counting distinct fluorescent foci per cell, with background signals subtracted.

Statistical analysis

All statistical analyses were performed using GraphPad Prism software 10. Data are presented as mean ± standard error of the mean (SEM). Statistical significance was assessed using an unpaired, two-tailed Student's *t*-test for single comparisons and one-way ANOVA followed by Tukey's multiple-comparisons test for multiple comparisons. Statistical details (e.g., number of animals per group) are provided in the figure legends. P values less than 0.05 were considered statistically significant.

Results

Eosinophil deficiency alters the monocyte/macrophage compartment in the bone marrow and peritoneal tissue niche

To define the role of eosinophils and their mediators in shaping macrophage function, we first characterized steady-state changes in monocyte and macrophage populations in an eosinophil-deficient model using single-cell RNA sequencing (scRNA-seq) and spectral flow cytometry. First, we analyzed the bone marrow, the primary postnatal source of monocytes and macrophages (24). $CD45^+$ hematopoietic cells were isolated from ΔdblGATA eosinophil-deficient mice and WT controls and subjected to 10× Genomics scRNA-seq (Fig. 1A). Cluster annotation and cell type identification visualized via UMAP revealed a significant increase in activated neutrophils and a reduction in cell cycle–active B cells in ΔdblGATA mice as compared to WT controls (Fig. 1B, C; Fig. S1A). Notably, differential gene expression (DEG) analysis and KEGG pathway enrichment in all cells revealed osteoclast differentiation as the top enriched pathway in eosinophil-deficient mice compared to WT controls (Fig. S1B, C).

Within the monocyte/macrophage compartment, only minor changes in population frequencies were observed, with a slight increase in monocytes and a corresponding decrease in osteoclast precursors and macrophages in ΔdblGATA mice as compared to WT controls (Fig.

1D, E). However, further molecular characterization of the identified subclusters via DEG analysis and KEGG pathway enrichment analysis revealed an enhanced inflammatory gene signature (Fig. S1D, E). Importantly, analysis of the top differentially regulated transcription factors (TFs) revealed that eosinophil loss led to upregulation of IFN signaling and inflammation-associated TFs, resembling a transcriptional profile of classically activated macrophages (CAM), while TFs involved in alternative macrophage polarization, such as *Pparg*, were downregulated (Fig. 1F). These findings indicate that eosinophil loss induces a more activated and pro-inflammatory state in bone marrow monocytes and macrophages. These findings were confirmed by spectral flow cytometry, which revealed an increased abundance of neutrophils, whereas the numbers of monocytes and macrophages remained unchanged. However, macrophages exhibited a more inflammatory phenotype, characterized by increased MHC-II expression (Fig. 1G, H).

To characterize the impact of eosinophil loss on tissue-resident macrophages, we analyzed $CD45^+$ cells within the peritoneal cavity, containing two distinct macrophage populations: large peritoneal macrophages (LPMs), representing the embryonically derived, long-lived resident population, and small peritoneal macrophages (SPMs), which are monocyte-derived, short-lived, and predominantly expand during inflammatory conditions (25). $CD45^+$ cells were isolated from ΔdblGATA eosinophil-deficient mice and WT controls and subjected to 10× Genomics scRNA-seq (Fig. 2A). Cluster annotation and cell type identification visualized via UMAP revealed a significant shift in the B cell compartment in eosinophil-deficient mice compared to WT controls, characterized by an increased proportion of B1 cells and a concomitant reduction in B2 cells. Furthermore, a decreased frequency of T cells was observed following eosinophil depletion (Fig. 2B–D).

As expected, we identified two distinct macrophage populations in the peritoneum, designated as LPMs and SPMs according to their top differentially expressed genes and signature score assessment (Fig. 2B-F; Fig. S2A, B). While the SPM population remained largely unchanged, LPMs were nearly doubled in ΔdblGATA mice compared to WT controls (Fig. 2B–D). Transcriptional profiling of these subtypes in ΔdblGATA versus WT mice revealed a heightened inflammatory signature in both populations. This was reflected in the top differentially regulated TFs, including *Hif1a*, *Nfkb1*, *Stat3*, *Jun*, and *Foxl2* (Fig. 2G, H, J, K). Consistent with this, KEGG pathway analysis highlighted significant enrichment of pro-inflammatory pathways, including the IL-17 signaling pathway, NF-κB signaling pathway, TNF signaling pathway, and chemokine signaling pathway, as well as associations with various inflammatory diseases (Fig. 2I, L). These inflammatory signatures were not limited to the individual subtypes but were also evident when analyzing the entire monocyte/macrophage compartment in the peritoneum, as well as the combined populations of LMP and SPM (Fig. S2C–H). Intriguingly, in SPMs, pathways related to proteasome function and oxidative phosphorylation were significantly downregulated in the absence of eosinophils (Fig. 2L), suggesting a metabolic shift toward a more inflammatory state. Although spectral flow cytometry revealed no significant changes in the proportions of LPMs or SPMs, SPMs from ΔdblGATA mice exhibited increased expression of the pro-inflammatory activation marker CD80 (Fig. 2M–O).These data support the notion that eosinophils also regulate the numbers and functional state of tissue niche–derived macrophages, altering their composition and, similar to what has been observed in the bone marrow, promoting a more activated and inflammatory macrophage compartment.

Eosinophil peroxidase (EPX) induces a time-dependent shift in macrophage polarization from pro-inflammatory to alternatively activated phenotype

Eosinophil-derived cytokines such as IL-4 and IL-13 are well established as drivers of anti-inflammatory, alternative activated macrophage polarization, particularly in adipose tissue and during tissue injury (13, 26, 27). However, these cytokines are typically expressed at low levels in eosinophils under steady-state conditions and require an external stimulus for robust production. Given that ΔdblGATA mice are completely deficient in both eosinophils and EPX, this enzyme, which is expressed in large amounts in eosinophils also under steady-state conditions, emerges as a strong candidate underlying the observed shift in macrophage phenotype in the absence of eosinophils.

To investigate the potential influence of EPX on macrophage polarization, we stimulated bone marrow-derived macrophages for 24 hours with EPX as compared with the classical macrophage-inducing mediators LPS and IFN-γ and the AAM-stimulating cytokine IL-4 (Fig. 3A). Flow cytometric analysis revealed that LPS+IFN-γ treatment promoted a CAM phenotype characterized by high levels of MHC-II and CD86 expression. In contrast, EPX stimulation resulted in significant upregulation of alternative activation marker proteins, including PD-L2 and CD206 (Fig. 3B, C). This effect could also be confirmed at the transcriptional level, showing *Nos2* and *Il1b* expression exclusively in LPS stimulated macrophages (Fig. 3D). Similarly, immunofluorescence staining showed increased CD86 expression predominantly in cells stimulated with LPS (Fig. 3E, F). Morphologically, EPX-stimulated macrophages exhibited a distinct appearance compared to LPS-activated classical macrophages, displaying an elongated, spindle-like morphology that resembled the phenotype associated with alternative activation induced by IL-4 (Fig. 3G). When examining cytokine secretion, LPS+IFN-γ-stimulated macrophages produced the highest levels of the pro-inflammatory cytokines IL-1β, TNFα, and IL-6. In contrast, EPX failed to induce IL-1β but induced the secretion of TNFα, IL-6, as well as the anti-inflammatory cytokine IL-10 (Fig. 3H). These findings suggest that EPX may play a dual role: initially promoting inflammation, but potentially driving macrophages toward an anti-inflammatory phenotype upon subsequent exposure.

To characterize the temporal dynamics of EPX-induced macrophage polarization, we performed bulk RNA sequencing at 8- and 24- hours following stimulation (Fig. 4A). Transcriptomic analysis revealed that EPX profoundly reshapes the macrophage gene expression landscape at both time points (Fig. 4A-C). Early EPX stimulation (8 hours) was associated with a predominantly pro-inflammatory transcriptional profile, marked by increased expression of *Nfkb1*, *Il1b*, *Il6*, *Cd86*, and *Tnf*. Concurrently, some AAM-associated genes, including *Ccl17*, *Ccl22*, *Il4ra*, and *Il10*, were already upregulated. In contrast, prolonged EPX exposure (24 hours) was characterized by a reduction in pro-inflammatory gene expression and a marked increase in *Arg1* and *Retnla* expression (Fig. 4D-F).

Comparison of EPX- and LPS-stimulated macrophages further demonstrated that EPX exposure induces both inflammatory and alternative activation characteristics (Fig. S3A-C). Notably, an alternative activation signature became apparent after 24 hours of EPX stimulation, with significant upregulation of genes including *Cd36*, *Lgals3*, *Il10*, and *Retnla*, in comparison to LPS-stimulated macrophages (Fig. S3D, E). Consistent with these findings, GO enrichment analysis revealed a strong enrichment of phagocytosis-related pathways in EPX- compared with LPS-stimulated macrophages (Fig. S3F).

In contrast, EPX-induced gene expression remained clearly distinct from that induced by IL-4 at both time points (Fig. S4A-C). While IL-4 stimulation led to high expression of typical AAM-associated genes such as *Mrc1*, *Cd163*, and *Chil3*, EPX treatment resulted in upregulation of

Arg1, *Il4ra*, *Il10*, and *Stab1* (Fig. S4D, E). GO enrichment analysis indicated a more pronounced macrophage-activating response following 24 hours of EPX stimulation compared to IL-4. (Fig. S4F). These findings indicate that although prolonged EPX stimulation promotes an AAM-like phenotype, the resulting transcriptional program differs substantially from classical IL-4-driven alternative macrophage activation. These findings demonstrate that EPX induces a dynamic macrophage response, characterized by an early pro-inflammatory state followed by a shift toward an anti-inflammatory, pro-resolving phenotype.

EPX promotes metabolic flexibility and redox adaptation in macrophages

Recent studies have emphasized the importance of metabolic states in macrophage polarization and function. Pro-inflammatory macrophages predominantly rely on glycolysis for energy, while AAMs depend mainly on OXPHOS (28). Bulk RNA sequencing and extracellular flux analyses confirmed that LPS stimulation shifts macrophage metabolism toward glycolysis, whereas IL-4-treated AAMs exhibit high OXPHOS (Fig. 5A-H). Interestingly, EPX-treated macrophages showed increased levels of both glycolysis and OXPHOS (Fig. 5A-H). Concurrent upregulation of glycolysis and OXPHOS suggests that EPX induces a metabolically flexible macrophage phenotype with high bioenergetic and biosynthetic capacity, rather than a canonical inflammatory or IL-4-induced alternatively activated state.

Mitochondrial activity and redox regulation are key determinants of macrophage activation states. Unlike LPS stimulation, which resulted in sustained elevation of mitochondrial mass and mitochondrial reactive oxygen species (ROS) production, EPX induced a transient increase in mitochondrial content and oxidative activity during the early phase of activation (Fig. 5I, J). This early mitochondrial response coincided with the induction of redox-regulatory genes, including *Hmox1* and *Prdx1*, suggesting that EPX triggers an adaptive antioxidant program to maintain redox balance (Fig. 5K, L). By 24 hours after stimulation, mitochondrial ROS levels and mass returned to baseline, indicating effective resolution of the initial oxidative response rather than persistent mitochondrial stress (Fig. 5I, J). Thus, EPX drives a controlled mitochondrial adaptation that enables an initial inflammatory response while preventing chronic oxidative stress and supporting subsequent phenotypic reprogramming.

EPX induces transcriptional and functional reprogramming toward enhanced efferocytosis in macrophages

An energy-demanding function of pro-resolving macrophages is the clearance of apoptotic cells, a process known as efferocytosis. We therefore investigated whether EPX influences the efferocytic capacity of macrophages compared with LPS- and IL-4-induced activation. Bulk RNA sequencing analysis revealed that EPX-treated macrophages upregulated a broad set of efferocytosis-associated genes at both 8 and 24 hours after stimulation (Fig. 6A, B). Consistently, flow cytometric analysis demonstrated increased expression of key efferocytic receptors, including CD36, TREM2, and CD93, following EPX stimulation (Fig. 6C, D). In line with these transcriptional and phenotypic changes, EPX-treated macrophages exhibited a markedly enhanced capacity to engulf apoptotic neutrophils, as demonstrated by flow cytometry and live-cell imaging (Fig. 6E-G; Movie S1-4). These findings identify enhanced efferocytosis as a prominent functional feature of the EPX-induced macrophage phenotype and suggest a shift toward an inflammation-resolving macrophage state.

EPX counteracts LPS/IFN-γ–induced inflammation

We next investigated whether this anti-inflammatory pro-resolving macrophage signature by induced by EPX is sustained under inflammatory conditions mimicking those found in chronic inflammatory diseases. To address this, we evaluated macrophage responses to combined stimulation with LPS and IFN-γ with or without concurrent EPX treatment (Fig. S5). Strikingly, co-treatment with EPX significantly dampened the pro-inflammatory response induced by LPS+IFN-γ. At the mRNA level, expression of *Nos2*, a hallmark of inflammatory activation, was markedly reduced, while genes associated with resolution, including *Acod1* and *Il10*, were significantly upregulated (Fig. S5A). Consistent with these findings, the expression of key pro-inflammatory surface markers, MHC-II and CD86, was strongly suppressed in the presence of EPX (Fig. S5B). On the metabolic level, EPX treatment partially restored OXPHOS that had been impaired by LPS+IFN-γ stimulation, indicating a protective or restorative effect on macrophage bioenergetics (Fig. S5C, D). Furthermore, analysis of secreted cytokines revealed a clear shift in the inflammatory profile: levels of classical pro-inflammatory mediators such as TNFα and IL-6 were significantly reduced, whereas secretion of AAM-associated cytokines, including CCL22, CCL17, and IL-10, was markedly enhanced in the presence of EPX (Fig. S5E, F). Collectively, these results demonstrate that EPX can actively reprogram LPS+IFN-γ-activated macrophages, counteracting inflammatory signaling and promoting a pro-resolving phenotype. This highlights the potential of EPX to modulate macrophage function in inflammatory environments.

EPX is internalized following CD11b-dependent binding

Given the broad effects of EPX on macrophage activation, metabolism, and efferocytotic functions, we aimed to uncover potential mechanisms underlying EPX recognition by macrophages. CD11b (integrin αM, encoded by *Itgam*) is a highly expressed myeloid surface receptor involved in ligand recognition, phagocytosis, and regulation of macrophage activation states. Based on its established role in sensing extracellular ligands and coordinating immune cell effector functions, we investigated whether CD11b contributes to EPX–macrophage interactions. This was further supported by previous reports demonstrating that CD11b can induce endocytic uptake in macrophages (29) and by evidence that myeloperoxidase (MPO), a structurally related heme peroxidase, mediates cellular responses through CD11b signaling (30). Bulk RNA sequencing revealed that genes associated with CD11b signaling were preferentially upregulated following 8 hours of EPX stimulation compared with 24 hours, suggesting an early involvement of this pathway in EPX-mediated macrophage activation (Fig. 7A). Confocal microscopy of fluorescently labeled EPX and CD11b demonstrated partial co-localization on macrophages (Fig. 7B). Furthermore, internalized EPX co-localized with CD11b within macrophages, indicating that CD11b may contribute to EPX uptake or intracellular trafficking (Fig. 7C; Movie S5). To further investigate the association between EPX and CD11b, we performed a proximity ligation assay (PLA), which demonstrated close spatial proximity between EPX and CD11b in macrophages (Fig. 7D). Finally, to assess the functional relevance of CD11b in EPX-induced macrophage reprogramming, macrophages were stimulated with EPX in the presence of a neutralizing anti-CD11b antibody as compared to an isotype control (Fig. 7E). CD11b inhibition significantly attenuated the EPX-induced upregulation of the AAM-associated surface markers PD-L2, CD163, and TREM2 as compared with the isotype control (Fig. 7F), indicating that CD11b contributes to EPX-mediated macrophage polarization.

Systemic and intranasal EPX administration both attenuate inflammation in LPS-induced lung injury

To determine whether the *in vitro* immunomodulatory effects of EPX translate to an *in vivo* setting, we employed an LPS-induced acute lung injury (ALI) model in conjunction with EPX treatment. On day 0, BALB/c mice were challenged with 40 µg of LPS via intranasal (i.n.) administration, followed by intravenous (i.v.) administration of 40 µg EPX on days 0 and 2 (Fig. 8A). Lung inflammation was evaluated at two time points: day 1 (peak inflammatory phase) and day 3 (resolution phase). EPX treatment significantly attenuated lung inflammation, as demonstrated by histological analysis using H&E staining, which revealed reduced inflammatory infiltrates and tissue damage (Fig. 8B). This protective effect was associated with an increased frequency of PD-L2-positive macrophages in lung tissue, suggesting a shift toward a pro-resolving or regulatory macrophage phenotype (Fig. 8C, D). Consistent with reduced inflammation, neutrophil infiltration was markedly decreased in the lungs of EPX-treated mice at both day 1 and day 3 post-LPS challenge (Fig. 8E-G). Analysis of lung-resident macrophage subsets revealed dynamic changes in response to LPS and EPX. Interstitial macrophages were significantly expanded at day 1 post-LPS in control mice, but this increase was absent in the LPS+EPX group, suggesting EPX may modulate early macrophage recruitment or differentiation (Fig. 8F). By day 3, however, both LPS and LPS+EPX groups showed elevated interstitial macrophage numbers, indicating that EPX does not prevent the later accumulation of these cells (Fig. 8G). Alveolar macrophages were partially reduced one day after LPS administration in the LPS-only group but were unchanged in the LPS+EPX group (Fig. 8F). At day 3, alveolar macrophage numbers were markedly diminished in LPS-treated mice, but this loss was slightly attenuated in the EPX co-treatment group, suggesting EPX helps preserve alveolar macrophage homeostasis during resolution (Fig. 8G). Systemic cytokine analysis revealed that serum levels of key pro-inflammatory mediators, including TNFα, IFN-γ, and IL-6 were significantly lower in the LPS+EPX group compared to the LPS-only group at day 1 (Fig. 8H). A similar trend was observed at day 3, although overall cytokine levels had declined across all groups, consistent with the natural resolution of inflammation (Fig. 8I).

To investigate the local effects of EPX in the lung, we employed an LPS-induced ALI model combined with i.n. administration of 10 µg EPX, with a particular focus on the resolution phase at day 3 (Fig. S6A). Similar to systemic EPX administration, local delivery of EPX attenuated lung inflammation, as evidenced by reduced pathology in H&E-stained lung sections and a corresponding decrease in the lung injury score (Fig. S6B, C). Spectral flow cytometry analysis of lung immune cell composition at day 3 revealed no significant differences in neutrophil numbers between the LPS-only and LPS+EPX groups. However, monocyte recruitment was markedly reduced in mice receiving EPX in addition to LPS, compared to those treated with LPS alone (Fig. S6D, E). The overall abundance of interstitial macrophages was not altered; however, EPX treatment shifted their activation state, resulting in a higher proportion of alternatively activated (MHC-II^{-}CD206^{+}) compared with classically activated (MHC-II^{+}CD206^{-}) interstitial macrophages relative to LPS treatment alone (Fig. S6D, E). Consistent with the effects observed following systemic EPX administration, local EPX treatment slightly restored the markedly reduced alveolar macrophage population induced by LPS challenge (Fig. S6D, E). Notably, while LPS alone led to a significant reduction in pulmonary eosinophils, local EPX administration effectively reversed this loss, pointing to a potential positive feedback loop in which EPX helps maintain eosinophil numbers in the lung niche (Fig. S6D, E).

Together, these findings demonstrate that systemic and local EPX treatments exert potent anti-inflammatory effects *in vivo*, modulating macrophage functions and systemic cytokine responses during acute lung injury. These results further highlight the role of eosinophils in restoring tissue homeostasis following lung inflammation.

Discussion

Our study reveals a previously unrecognized immunomodulatory function of EPX in driving macrophage-mediated resolution of inflammation. EPX has long been associated with cytotoxic and pro-inflammatory effects during eosinophilic inflammation(18). Our findings show that EPX initially induces a pro-inflammatory macrophage phenotype, but over time orchestrates a shift toward a pro-resolving state through coordinated metabolic, signaling, and functional reprogramming. This dual role—initially pro-inflammatory yet ultimately essential for resolution—positions EPX as a key molecular switch in the transition from inflammation to tissue repair.

Evidence for the immune-regulatory functions of EPX remains sparse, with only limited reports implicating it in processes such as extracellular matrix remodeling and angiogenesis (31, 32). In our previous work on inflammatory bone loss, we identified a direct influence of EPX on the osteoclast lineage, indicating its broader role in immune modulation (33, 34). In contrast, the anti-inflammatory potential of myeloperoxidase (MPO), a structurally and mechanistically similar heme peroxidase secreted by neutrophils, is far better characterized. Studies in both mice and humans indicate that MPO deficiency can worsen inflammation in certain contexts. For example, MPO-deficient mice exhibit exacerbated neutrophil accumulation and delayed resolution in models of acute lung inflammation (35-37), while in experimental arthritis, they develop more severe disease due to heightened dendritic cell activation and enhanced $CD4^+$ T cell responses in lymph nodes (30). Although MPO deficiency in human is often clinically silent, it has been associated with increased infection susceptibility and chronic inflammatory conditions (38). Notably, loss-of-function mutations in MPO are linked to generalized pustular psoriasis, likely due to impaired clearance of neutrophils by macrophages and prolonged neutrophil persistence in inflamed tissues (39). Despite these findings, a direct role of MPO in modulating macrophage polarization has not yet been investigated, representing a compelling and underappreciated avenue for future research. Such comparative studies could reveal conserved or divergent mechanisms by which heme peroxidases shape innate immune responses.

Single-cell RNA sequencing uncovered that eosinophil deficiency leads to a dysregulated monocyte/macrophage compartment in both bone marrow and peritoneal niches, characterized by heightened inflammatory gene signatures. This observation suggests that eosinophils maintain a baseline regulatory tone in myeloid cells even under steady-state conditions and strongly align with the Local Immunity And/or Remodeling/Repair (LIAR) hypothesis of James Lee, proposing that eosinophils are intrinsically homeostatic cells that actively contribute to tissue equilibrium and adapt to their local microenvironment (40). Accumulating evidence supports this homeostatic role across multiple tissues, most notably in the gut, adipose tissue, liver, and lungs (4, 13, 26, 41-45). Our study reveals that the eosinophil-derived protein EPX ameliorates lung inflammation. This is in line with the study of Zhu et al. reporting exacerbated ALI in eosinophil-deficient PHIL mice and identified CD101-negative eosinophils as suppressors of ALI (46). Collectively, these findings highlight the role of eosinophils in regulating inflammation and restoring tissue homeostasis.

The anti-inflammatory and tissue-repairing functions of eosinophils have previously been attributed to their secretion of IL-4, which promotes alternative macrophage activation through STAT6 signaling (47). Although EPX-treated macrophages share several features with IL-4-polarized macrophages, including expression of characteristic surface markers, anti-inflammatory cytokine production, and enhanced efferocytosis, our findings demonstrate that EPX induces a distinct macrophage activation program. Rather than directly promoting an alternatively activated phenotype, EPX elicits a time-dependent reprogramming characterized by an early transient inflammatory transcriptional response that subsequently transitions into a pro-resolving, highly efferocytotic phenotype. This phenotypic switch is accompanied by profound metabolic remodeling. EPX promotes metabolic flexibility through the concurrent activation of glycolysis and oxidative phosphorylation, supporting the high energetic demands of macrophage activation and efferocytosis. In parallel, EPX induces a tightly controlled redox response, characterized by transient mitochondrial activation followed by the upregulation of antioxidant pathways, including *Hmox1* and *Prdx1*. This adaptive response restores mitochondrial homeostasis and contrasts with the sustained mitochondrial ROS accumulation observed following LPS stimulation (48). Together, these findings suggest that EPX controls mitochondrial remodeling rather than inducing persistent oxidative stress, thereby facilitating macrophage adaptation toward a resolution-associated phenotype.

A defining functional consequence of EPX stimulation is the marked enhancement of efferocytosis, a key process required for the clearance of apoptotic cells, termination of inflammation, and tissue repair (49). The induction of efferocytotic receptors, including CD36, TREM2, and CD93, together with increased uptake of apoptotic neutrophils, provides a mechanistic link between EPX-mediated metabolic reprogramming and inflammation resolution. Furthermore, our data identify CD11b as a critical mediator of EPX-induced macrophage activation. The close spatial association between EPX and CD11b and the attenuation of macrophage reprogramming following CD11b blockade suggest that CD11b serves as an important recognition and signaling receptor for EPX, highlighting a previously unrecognized receptor-ligand axis in macrophage regulation. This is consistent with the finding that the structurally related heme peroxidase MPO also signals through CD11b to regulate dendritic cell function, suggesting a broader role for CD11b as a key receptor for heme peroxidases in innate immune cell modulation (30).

In ALI, the anti-inflammatory effects of EPX have also been attributed to its ability to modulate macrophage responses. In this disease, the functional dynamics of lung-resident macrophage subtypes, particularly alveolar macrophages and interstitial macrophages, are central to disease progression and resolution. Alveolar macrophages, derived from embryonic precursors and maintained through local self-renewal, are inherently tissue-protective under homeostatic conditions, contributing to immune surveillance, surfactant homeostasis, and the suppression of inappropriate inflammation. However, during inflammation, alveolar macrophages are rapidly depleted or functionally impaired due to apoptosis, cell shedding, or phenotypic reprogramming, leading to a loss of their protective barrier function and a consequent increase in susceptibility to injury (50, 51). In contrast, interstitial macrophages, predominantly monocyte-derived and more plastic, respond to tissue damage by adopting a pro-inflammatory phenotype, amplifying inflammation through cytokine release and neutrophil recruitment. Yet, interstitial macrophages also possess a remarkable capacity for functional reprogramming: as inflammation resolves, they are transcriptionally, epigenetically, and functionally conditioned by the airway environment to take on alveolar macrophage identity (50). EPX administration slowed the loss of the alveolar macrophage compartment while

limiting the expansion of inflammatory interstitial macrophages. This macrophage reprogramming was accompanied by reduced systemic pro-inflammatory cytokine production, decreased neutrophil recruitment to the lung, and attenuation of pulmonary inflammation and tissue damage. This is in line with our previous study, which demonstrated that EPX not only mitigates inflammatory arthritis-induced bone loss but also promotes more rapid disease resolution (33). Future studies are needed to determine whether this EPX-driven regulatory pathway also contributes to the resolution of chronic inflammatory diseases.

Collectively, our findings expand the current understanding of eosinophil biology by identifying EPX as an immunoregulatory mediator that actively drives macrophage reprogramming. Beyond its established role as a cytotoxic granule protein, EPX promotes resolution of inflammation through coordinated regulation of macrophage metabolism, mitochondrial homeostasis, and efferocytotic function via CD11b-dependent signaling. These findings reveal a previously unrecognized mechanism by which eosinophil-derived mediators promote macrophage adaptation and link eosinophil activity to tissue repair and resolution of inflammation.

Acknowledgements

We gratefully acknowledge Franceska Jelas, Forough Saberian, Christine Zech, Barbara Happich, and Bianca Bazylak-Kaps for their excellent technical support. We thank our colleagues Baraka Favored, Katerina Kachler, and Thamer Al-Hamad for their experimental support during the large-scale *in vivo* experiments. We thank Uwe Appelt and Markus Mroz from the Core Unit Cell Sorting and Immunomonitoring for their expert assistance with flow cytometry and cell sorting. We also extend our thanks to Arif Ekici of the NGS Core Unit for his valuable support in single-cell RNA sequencing. Finally, we strongly appreciate the assistance provided by Philipp Tripal from the Optical Imaging Centre Erlangen in confocal microscopy.

Funding

This study was supported by:

The German Research Foundation/Deutsche Forschungsgemeinschaft (DFG) – project AN 1917/3-1 (DA) and BO 3811/18-1 (AB) (591247085)

The DFG - Collaborative Research Center (CRC)/Transregio 369 (DIONE-501752319) project B03 (DA), project B05 (AB), and project A02 (AB)

The DFG - CRC 1755 (CASCAID-550296805) projects 01 and project 11 (AB)

The Leibniz Prize (GS)

The ERC Consolidator Grant ODE (AB)

The Interdisciplinary Center for Clinical Research (IZKF) grant J90 (DA) and A77 (AB)

The Boehringer Ingelheim Stiftung Exploration Grant (DA)

Author contributions

Conceptualization: AB, DA

Methodology: LTAM, MS, PP, MAK, RP, AR, YH, JPA, DA

Investigation: LTAM, MS, PP, MAK, RP, AR, YH, JPA, DA

Visualization: LTAM, MS, PP, MAK, RP, AR, DA

Funding acquisition: GS, AB, DA
Project administration: AB, DA
Supervision: AB, DA
Writing – original draft: DA
Writing – review & editing: LTAM, MS, PP, MAK, RP, AR, YH, JPA, GK, GS, AB, DA

Conflict of interest

The authors declare that the research was conducted without any commercial or financial relationships that could be perceived as a potential conflict of interest.

Data and materials availability

All original sequencing data (fastq files) have been deposited in the GEO database under the accession code GSE348040, GSE347683, and GSE347419. All other data are available from the corresponding author upon reasonable request.

References

1. Rosenberg HF, Dyer KD, Foster PS. Eosinophils: changing perspectives in health and disease. Nat Rev Immunol. 2013;13(1):9-22.
2. Acharya KR, Ackerman SJ. Eosinophil granule proteins: form and function. J Biol Chem. 2014;289(25):17406-15.
3. Weller PF, Spencer LA. Functions of tissue-resident eosinophils. Nat Rev Immunol. 2017;17(12):746-60.
4. Arnold IC, Munitz A. Spatial adaptation of eosinophils and their emerging roles in homeostasis, infection and disease. Nat Rev Immunol. 2024.
5. Ginhoux F, Guilliams M. Tissue-Resident Macrophage Ontogeny and Homeostasis. Immunity. 2016;44(3):439-49.
6. Guan F, Wang RX, Yi ZJ, Luo P, Liu WY, Xie Y, et al. Tissue macrophages: origin, heterogenity, biological functions, diseases and therapeutic targets. Signal Transduct Tar. 2025;10(1).
7. Kuznetsova T, Prange KHM, Glass CK, de Winther MPJ. Transcriptional and epigenetic regulation of macrophages in atherosclerosis. Nat Rev Cardiol. 2020;17(4):216-28.
8. Murray PJ. Macrophage Polarization. Annu Rev Physiol. 2017;79:541-66.
9. Osorio-Valencia S, Zhou BS. Roles of Macrophages and Endothelial Cells and Their Crosstalk in Acute Lung Injury. Biomedicines. 2024;12(3).
10. Faas M, Ipseiz N, Ackermann J, Culemann S, Gruneboom A, Schroder F, et al. IL-33-induced metabolic reprogramming controls the differentiation of alternatively activated macrophages and the resolution of inflammation. Immunity. 2021;54(11):2531-46 e5.
11. Schett G, Neurath MF. Resolution of chronic inflammatory disease: universal and tissue-specific concepts. Nature Communications. 2018;9.
12. Wculek SK, Dunphy G, Heras-Murillo I, Mastrangelo A, Sancho D. Metabolism of tissue macrophages in homeostasis and pathology. Cell Mol Immunol. 2022;19(3):384-408.
13. Wu D, Molofsky AB, Liang HE, Ricardo-Gonzalez RR, Jouihan HA, Bando JK, et al. Eosinophils sustain adipose alternatively activated macrophages associated with glucose homeostasis. Science. 2011;332(6026):243-7.
14. Kolbinger A, Schäufele TJ, Steigerwald H, Friedel J, Pierre S, Geisslinger G, et al. Eosinophil-derived IL-4 is necessary to establish the inflammatory structure in innate inflammation. Embo Mol Med. 2023;15(2).
15. Chen Z, Andreev D, Oeser K, Krljanac B, Hueber A, Kleyer A, et al. Th2 and eosinophil responses suppress inflammatory arthritis. Nat Commun. 2016;7:11596.

16. Andreev D, Liu M, Kachler K, Llerins Perez M, Kirchner P, Kolle J, et al. Regulatory eosinophils induce the resolution of experimental arthritis and appear in remission state of human rheumatoid arthritis. Ann Rheum Dis. 2021;80(4):451-68.
17. Yang Y, Xu L, Atkins C, Kuhlman L, Zhao J, Jeong JM, et al. Novel IL-4/HB-EGF-dependent crosstalk between eosinophils and macrophages controls liver regeneration after ischaemia and reperfusion injury. Gut. 2024;73(9):1543-53.
18. Wang J, Slungaard A. Role of eosinophil peroxidase in host defense and disease pathology. Arch Biochem Biophys. 2006;445(2):256-60.
19. Roth-Carter QR, Kornfield J, Luo H, Ochkur SI, Jacobsen EA, Fryer AD, et al. Eosinophil peroxidase induces inflammation in a mouse model of dermatitis. J Leukoc Biol. 2025;118(1).
20. Chu DK, Jimenez-Saiz R, Verschoor CP, Walker TD, Goncharova S, Llop-Guevara A, et al. Indigenous enteric eosinophils control DCs to initiate a primary Th2 immune response in vivo. J Exp Med. 2014;211(8):1657-72.
21. Zabucchi G, Menegazzi R, Cramer R, Nardon E, Patriarca P. Mutual Influence between Eosinophil Peroxidase (Epo) and Neutrophils - Neutrophils Reversibly Inhibit Epo Enzymatic-Activity and Epo Increases Neutrophil Adhesiveness. Immunology. 1990;69(4):580-7.
22. Yu C, Cantor AB, Yang H, Browne C, Wells RA, Fujiwara Y, et al. Targeted deletion of a high-affinity GATA-binding site in the GATA-1 promoter leads to selective loss of the eosinophil lineage in vivo. J Exp Med. 2002;195(11):1387-95.
23. Culemann S, Gruneboom A, Nicolas-Avila JA, Weidner D, Lammle KF, Rothe T, et al. Locally renewing resident synovial macrophages provide a protective barrier for the joint. Nature. 2019;572(7771):670-5.
24. Lazarov T, Juarez-Carreno S, Cox N, Geissmann F. Physiology and diseases of tissue-resident macrophages. Nature. 2023;618(7966):698-707.
25. Cassado Ados A, D'Imperio Lima MR, Bortoluci KR. Revisiting mouse peritoneal macrophages: heterogeneity, development, and function. Front Immunol. 2015;6:225.
26. Goh YP, Henderson NC, Heredia JE, Red Eagle A, Odegaard JI, Lehwald N, et al. Eosinophils secrete IL-4 to facilitate liver regeneration. Proc Natl Acad Sci U S A. 2013;110(24):9914-9.
27. Heredia JE, Mukundan L, Chen FM, Mueller AA, Deo RC, Locksley RM, et al. Type 2 innate signals stimulate fibro/adipogenic progenitors to facilitate muscle regeneration. Cell. 2013;153(2):376-88.
28. Russell DG, Huang L, VanderVen BC. Immunometabolism at the interface between macrophages and pathogens. Nature Reviews Immunology. 2019;19(5):291-304.
29. Yao X, Dong G, Zhu Y, Yan F, Zhang H, Ma Q, et al. Leukadherin-1-Mediated Activation of CD11b Inhibits LPS-Induced Pro-inflammatory Response in Macrophages and Protects Mice Against Endotoxic Shock by Blocking LPS-TLR4 Interaction. Front Immunol. 2019;10:215.
30. Odobasic D, Kitching AR, Yang Y, O'Sullivan KM, Muljadi RCM, Edgtton KL, et al. Neutrophil myeloperoxidase regulates T-cell-driven tissue inflammation in mice by inhibiting dendritic cell function. Blood. 2013;121(20):4195-204.
31. DeNichilo MO, Panagopoulos V, Rayner TE, Borowicz RA, Greenwood JE, Evdokiou A. Peroxidase Enzymes Regulate Collagen Extracellular Matrix Biosynthesis. American Journal of Pathology. 2015;185(5):1372-84.
32. Panagopoulos V, Zinonos I, Leach DA, Hay SIJ, Liapis V, Zysk A, et al. Uncovering a new role for peroxidase enzymes as drivers of angiogenesis. Int J Biochem Cell B. 2015;68:128-38.
33. Andreev D, Kachler K, Liu M, Chen Z, Krishnacoumar B, Ringer M, et al. Eosinophils preserve bone homeostasis by inhibiting excessive osteoclast formation and activity via eosinophil peroxidase. Nat Commun. 2024;15(1):1067.
34. Andreev D, Bozec A. New Insights into Bone Loss in RA. Osteologie. 2021;30(4):319-25.

35. Kremserova S, Perecko T, Soucek K, Klinke A, Baldus S, Eiserich JP, et al. Lung Neutrophilia in Myeloperoxidase Deficient Mice during the Course of Acute Pulmonary Inflammation. Oxid Med Cell Longev. 2016;2016.
36. Takeuchi K, Umeki Y, Matsumoto N, Yamamoto K, Yoshida M, Suzuki K, et al. Severe neutrophil-mediated lung inflammation in myeloperoxidase-deficient mice exposed to zymosan. Inflamm Res. 2012;61(3):197-205.
37. Homme M, Tateno N, Miura N, Ohno N, Aratani Y. Myeloperoxidase deficiency in mice exacerbates lung inflammation induced by nonviable. Inflamm Res. 2013;62(11):981-90.
38. Kutter D, Devaquet P, Vanderstocken G, Paulus JM, Marchal V, Gothot A. Consequences of total and subtotal myeloperoxidase deficiency: Risk or benefit? Acta Haematol-Basel. 2000;104(1):10-5.
39. Haskamp S, Bruns H, Hahn M, Hoffmann M, Gregor A, Löhr S, et al. Myeloperoxidase Modulates Inflammation in Generalized Pustular Psoriasis and Additional Rare Pustular Skin Diseases. Am J Hum Genet. 2020;107(3):527-38.
40. Lee JJ, Jacobsen EA, McGarry MP, Schleimer RP, Lee NA. Eosinophils in health and disease: the LIAR hypothesis. Clin Exp Allergy. 2010;40(4):563-75.
41. Gurtner A, Borrelli C, Gonzalez-Perez I, Bach K, Acar IE, Nunez NG, et al. Active eosinophils regulate host defence and immune responses in colitis. Nature. 2023;615(7950):151-7.
42. Ignacio A, Shah K, Bernier-Latmani J, Koller Y, Coakley G, Moyat M, et al. Small intestinal resident eosinophils maintain gut homeostasis following microbial colonization. Immunity. 2022;55(7):1250-67 e12.
43. Brigger D, Riether C, van Brummelen R, Mosher KI, Shiu A, Ding Z, et al. Eosinophils regulate adipose tissue inflammation and sustain physical and immunological fitness in old age. Nat Metab. 2020;2(8):688-702.
44. Fan Z, Kong M, Dong W, Dong C, Miao X, Guo Y, et al. Trans-activation of eotaxin-1 by Brg1 contributes to liver regeneration. Cell Death Dis. 2022;13(5):495.
45. Mesnil C, Raulier S, Paulissen G, Xiao X, Birrell MA, Pirottin D, et al. Lung-resident eosinophils represent a distinct regulatory eosinophil subset. J Clin Invest. 2016;126(9):3279-95.
46. Zhu C, Weng QY, Zhou LR, Cao C, Li F, Wu YF, et al. Homeostatic and early-recruited CD101(-) eosinophils suppress endotoxin-induced acute lung injury. Eur Respir J. 2020;56(5).
47. Lawrence T, Natoli G. Transcriptional regulation of macrophage polarization: enabling diversity with identity. Nat Rev Immunol. 2011;11(11):750-61.
48. Casey AM, Ryan DG, Prag HA, Chowdhury SR, Marques E, Turner K, et al. Pro-inflammatory macrophages produce mitochondria-derived superoxide by reverse electron transport at complex I that regulates IL-1β release during NLRP3 inflammasome activation. Nature Metabolism. 2025;7(3).
49. Doran AC, Yurdagul A, Jr., Tabas I. Efferocytosis in health and disease. Nat Rev Immunol. 2020;20(4):254-67.
50. Bain CC, MacDonald AS. The impact of the lung environment on macrophage development, activation and function: diversity in the face of adversity. Mucosal Immunol. 2022;15(2):223-34.
51. Shi T, Denney L, An H, Ho LP, Zheng Y. Alveolar and lung interstitial macrophages: Definitions, functions, and roles in lung fibrosis. J Leukoc Biol. 2021;110(1):107-14.

Figure Legends

Fig. 1. Eosinophils regulate the monocyte/macrophage compartment in the bone marrow. A) Schematic overview of single-cell RNA sequencing analysis of $CD45^+$ hematopoietic cells isolated from the bone marrow of WT and ΔdblGATA mice. **B)** Clustering annotation and **C)** cell type quantification based on UMAP visualization of all cells, comparing ΔdblGATA and WT mice. **D)** UMAP visualization and **E)** cell type quantification of osteoclast

precursor, monocyte, and macrophage populations, comparing ΔdblGATA and WT mice. **F)** Identification of top differentially regulated transcription factors (TFs) between the ΔdblGATA and WT groups. **G)** Gating strategy for spectral flow cytometry analysis to identify immune cell populations: neutrophils ($CD11b^+Ly6G^+$), eosinophils ($CD11b^+SiglecF^+$), monocytes ($CD11b^+Ly6C^{high}$), and macrophages ($CD11b^+F4/80^+MerTK^+$). **H)** Proportions of eosinophils, neutrophils, monocytes, and macrophages, as well as MHC-II MFI on macrophages, in ΔdblGATA and WT mice (n = 10). Statistical analysis of scRNAseq was performed using a $\log_2$ fold change threshold of 0.25 and adjusted p-values (Padj) < 0.05 to define significance. Data are presented as mean ± SEM. Statistical significance was determined by unpaired two-tailed Student's *t*-test. Asterisks indicate statistical significance: *p < 0.05, ***p < 0.001, ****p < 0.0001.

Fig. 2. Eosinophils regulate tissue-resident macrophages in the peritoneal niche. A) Schematic overview of single-cell RNA sequencing analysis of $CD45^+$ cells isolated from the peritoneal cavity of WT and ΔdblGATA mice. **B)** Clustering annotation and **C)** genotype-specific cell distribution, visualized via UMAP, showing the overall cellular landscape in WT versus ΔdblGATA mice. **D)** Cell type quantification based on UMAP clustering of all cells, comparing WT and ΔdblGATA groups. **E)** UMAP colored by the expression of large peritoneal macrophage (LPM)- associated genes *Gata6* and *Timd4*. **F)** UMAP colored by the expression of small peritoneal macrophage (SPM)- associated genes *H2-Ab1* and *Ccr2* .**G)** UMAP visualization of LPM, with clustering annotation. **H)** Identification of top differentially regulated transcription factors (TFs) in LPM between ΔdblGATA and WT mice. **I)** KEGG pathway enrichment analysis highlighting significantly activated pathways in LPM of ΔdblGATA mice compared to WT controls. **J)** UMAP visualization of SPM, with clustering annotation. **K)** Identification of top differentially regulated TFs in SPM between ΔdblGATA and WT mice. **L)** KEGG pathway enrichment analysis revealing both significantly activated and suppressed pathways in SPM of ΔdblGATA mice relative to WT controls. **M)** Gating strategy for spectral flow cytometry analysis to identify eosinophils ($CD11b^+SiglecF^+$), LPM ($CD11b^+F4/80^{high}MHC\text{-}II^{low}$) and SPM ($CD11b^+F4/80^{low}MHC\text{-}II^{high}$) in the peritoneum. **N)** Proportions of eosinophils, LPMs and SPMs in ΔdblGATA and WT mice (n = 5). **O)** CD80 and CD86 MFI on LPMs and SPMs in ΔdblGATA and WT mice (n = 5). Statistical analysis of scRNAseq was performed using a $\log_2$ fold change threshold of 0.25 and adjusted p-values (Padj) < 0.05 to define significance. Data are presented as mean ± SEM. Statistical significance was determined by unpaired two-tailed Student's *t*-test. Asterisks indicate statistical significance: *p < 0.05, **p < 0.01.

Fig. 3. EPX promotes an alternative activation-like (AAM-like) macrophage phenotype. A) Schematic illustration of bone marrow-derived macrophage (BMDM) stimulation with LPS (1 µg/mL), IFN-γ (0.1 µg/mL), IL-4 (0.1 µg/mL), EPX (0.1 µg/mL), or no stimulation (unstimulated control). **B)** Flow cytometry gating strategy used to analyze surface marker expression on BMDMs. **C)** Mean fluorescence intensity (MFI) of MHC-II, CD86, PD-L2, and CD206 in BMDMs 24 hours post-stimulation (n = 5). **D)** mRNA expression levels of *Nos2* and *Il1b* in BMDMs 24 hours after stimulation (n = 5). **E)** Representative immunofluorescence images of BMDMs stained for CD86–AF700, CD206–AF594, CD68–AF488, and DAPI. Scale bar: 10 µm. **F)** Quantification of CD86–AF700 signal intensity (MFI) from immunofluorescence images (n = 4). **G)** Representative confocal microscopy images of Cx3cr1-dtTomato-positive BMDMs 24 hours post-stimulation, captured at 63× magnification. Scale bar: 20 µm. **H)**

Cytokine levels (IL-1β, TNFα, IL-6, IL-10) measured in BMDM culture supernatants 24 hours post-stimulation (n = 5). Data are presented as mean ± SEM. Statistical significance was determined by one-way ANOVA followed by Tukey's multiple comparisons test. Asterisks indicate statistical significance: *p < 0.05, **p < 0.01, ***p < 0.001, ****p < 0.0001.

Fig. 4. EPX induces a time-dependent reprogramming of macrophage polarization. A) Principal component analysis (PCA) of BMDMs stimulated with 0.1 µg/mL EPX for 8 or 24 hours, compared to unstimulated controls at the same time points (n = 4). **B)** Volcano plot depicting differentially expressed genes (DEGs) between the 8-hour EPX-treated group and the 8-hour control group. **C)** Volcano plot comparing DEGs in the 24-hour EPX-treated group versus the 24-hour control group. **D)** Volcano plot comparing DEGs between the 8-hour and 24-hour EPX-treated groups. **E)** GO enrichment analysis comparing the 8-hour EPX-treated group to the 24-hour EPX-treated group. **F)** Heatmap displaying the expression of key classical and alternatively activated macrophage-associated genes in BMDMs following 8 or 24 hours of control or EPX treatment. Differential expression analysis was performed using a $\log_2$ fold change threshold of 1.0. P-values were adjusted using the Benjamini–Hochberg method to control the false discovery rate (FDR). Genes with an adjusted P-value (Padj) < 0.05 were considered significantly differentially expressed.

Fig. 5. EPX promotes metabolic flexibility and redox adaptation in macrophages. A) Heatmap of oxidative phosphorylation (OXPHOS)-related differentially expressed genes (DEGs) in BMDMs 8 hours after stimulation with 1 µg/mL LPS, 0.1 µg/mL IL-4, 0.1 µg/mL EPX, or in unstimulated controls (n = 4). **B)** Heatmap of OXPHOS-related DEGs in BMDMs 24 hours post-stimulation. **C)** Oxygen consumption rate (OCR) profiles of BMDMs measured 24 hours after stimulation (n = 4). **D)** Quantification of key mitochondrial respiration parameters: ATP production, maximal respiration, and spare respiratory capacity (n = 4). **E)** Heatmap of glycolysis-related DEGs in BMDMs 8 hours post-stimulation. **F)** Heatmap of glycolysis-related DEGs in BMDMs 24 hours post-stimulation. **G)** Extracellular acidification rate (ECAR) profiles of BMDMs 24 hours after stimulation (n = 4). **H)** Quantification of glycolytic parameters: basal glycolysis, glycolytic capacity, and glycolytic reserve (n = 4). **I)** Quantification of mitochondrial (mt) mass via mean fluorescence intensity (MFI) of MitoTracker Green staining in BMDMs at 4 and 24 hours post-stimulation (n = 4). **J)** Quantification of mitochondrial reactive oxygen species (mtROS) levels by MFI of MitoSOX Red staining at 4 and 24 hours post-stimulation (n = 4). **K)** Heatmap of redox-regulating DEGs in BMDMs 8 hours after stimulation. Data are presented as mean ± SEM. Statistical significance was determined by one-way ANOVA followed by Tukey's multiple comparisons test. Asterisks indicate statistical significance: *p < 0.05, **p < 0.01, ***p < 0.001, ****p < 0.0001.

Fig. 6. EPX enhances efferocytosis in macrophages. A) Heatmap of efferocytosis-related differentially expressed genes (DEGs) in BMDMs 8 hours after stimulation with 1 µg/mL LPS, 0.1 µg/mL IL-4, 0.1 µg/mL EPX, or in unstimulated controls (n = 4). **B)** Heatmap of efferocytosis-related DEGs in BMDMs 24 hours post-stimulation (n = 4). **C)** Representative flow cytometry histograms showing expression of efferocytosis receptors on BMDMs 24 hours post-stimulation. **D)** Mean fluorescence intensity (MFI) of key efferocytosis receptors CD36, TREM2, and CD93 in BMDMs 24 hours after stimulation (n = 5). **E)** Representative contour plots assessing internalization of apoptotic neutrophils labeled with pHrodo (a fluorescent dye that emits signal only upon acidification in phagolysosomes) after 3 hours of co-culture with BMDMs stimulated for 24 hours. Apoptosis was induced with staurosporine for 6 hours. **F)** Quantification of pHrodo-positive BMDMs, representing the proportion of macrophages that have engulfed apoptotic cells (n = 4). **G)** Confocal microscopy images of Cx3cr1-dtTomato-positive BMDMs 24 hours post-stimulation, co-cultured with carboxyfluorescein succinimidyl ester (CFSE)-labeled apoptotic neutrophils (induced by staurosporine), illustrating phagocytic uptake of apoptotic cells, acquired at 63× magnification. Scale bar: 20 µm. Data are presented as mean ± SEM. Statistical significance was determined by one-way ANOVA followed by Tukey's multiple comparisons test. Asterisks indicate statistical significance: *$p < 0.05$, ***$p < 0.001$, ****$p < 0.0001$.

Fig. 7. EPX interacts with macrophages via CD11b. A) Heatmap of CD11b pathway-related differentially expressed genes (DEGs) in BMDMs 8 and 24 hours after stimulation with 0.1 µg/mL EPX (n = 4). **B)** Confocal microscopy images of BMDMs treated with 0.1 µg/mL Atto 647N-labeled EPX for 24 hours, stained with anti-CD11b–AF488 (green) and DAPI (blue). Scale bar: 7 µm. **C)** Z-stack projection showing internalized EPX colocalized with CD11b, indicated by yellow signal and marked with white arrows. Scale bar: 3 µm. **D)** Proximity ligation assay (PLA) performed in EPX-treated BMDMs (24 hours) using primary antibodies against EPX and CD11b. Red fluorescent signals indicate direct protein–protein interactions. Scale bar: 10 µm. **E)** Representative dot plots showing CD11b surface expression in BMDMs treated with 0.1 µg/mL EPX alone or in combination with 5 µg/mL anti-CD11b antibody. **F)** Quantification of mean fluorescence intensity (MFI) for CD11b, CD86, PD-L2, CD163, and TREM2 in BMDMs treated with EPX (0.1 µg/mL) in the presence of 5 µg/mL anti-CD11b antibody or isotype control antibody, compared to unstimulated controls (n = 5). Data are presented as mean ± SEM. Statistical significance was determined by one-way ANOVA followed by Tukey's multiple comparisons test. Asterisks indicate statistical significance: *$p < 0.05$, **$p < 0.01$, ***$p < 0.001$, ****$p < 0.0001$.

Fig. 8. Intravenous EPX administration mitigates inflammation in LPS-induced acute lung injury. A) Schematic representation of the 40 µg LPS-induced acute lung injury model, established via intranasal (i.n.) administration on day 0, with or without concurrent intravenous (i.v.) treatment of 40 µg EPX on days 0 and 2 (n = 4–5). **B)** Hematoxylin and eosin (H&E) staining of lung sections at 1 and 3 days post-LPS inhalation, showing inflammatory infiltrates and tissue pathology. Scale bar: 100 µm. **C)** Quantification and **D)** representative immunofluorescence images of CD86 (green) and PD-L2 (red)–positive macrophages in lung tissue 1 day after LPS exposure. Scale bar: 50 µm. **E)** Gating strategy for spectral flow cytometry analysis to identify immune cell populations: neutrophils ($CD11b^+Ly6G^+$), eosinophils ($CD11b^+SiglecF^+$), monocytes ($CD11b^+Ly6C^+$), interstitial macrophages (IM;

CD11b^{+}F4/80^{+}), and alveolar macrophages (AM; CD11b^{-}CD11c^{+}SiglecF^{+}). **F)** Proportions of neutrophils, eosinophils, monocytes, IMs, and AMs in the lungs at day 1 post-LPS inhalation (n = 4–5). **G)** Proportions of the same immune cell populations at day 3 post-LPS inhalation (n = 4–5). **H)** Serum levels of pro-inflammatory cytokines TNFα, IFN-γ, and IL-6 measured 1 day after LPS challenge. **I)** Serum levels of TNFα, IFN-γ, and IL-6 measured 3 days after LPS challenge. Data are presented as mean ± SEM. Statistical significance was determined by one-way ANOVA followed by Tukey's multiple comparisons test. Asterisks indicate statistical significance: *$p < 0.05$, **$p < 0.01$, ***$p < 0.001$, ****$p < 0.0001$.

Supplementary Materials

Supplementary Figure Legends

Fig. S1. Single-cell RNA sequencing of CD45$^+$ hematopoietic cells from the bone marrow of ΔdblGATA mice versus WT controls. A) UMAP visualization of total cell distribution, comparing ΔdblGATA mice to WT controls. **B)** Volcano plot depicting differentially expressed genes (DEGs) across all cell populations between ΔdblGATA and WT mice. **C)** KEGG pathway enrichment analysis highlighting significantly upregulated pathways in ΔdblGATA mice relative to WT controls across all cells. **D)** Volcano plot showing DEGs within the osteoclast precursor, monocyte, and macrophage compartments comparing ΔdblGATA and WT mice. **E)** KEGG pathway enrichment analysis of differentially regulated pathways in the osteoclast precursor, monocyte, and macrophage compartment in ΔdblGATA mice versus WT controls, including both upregulated and downregulated pathways. Statistical analysis of scRNAseq was performed using a $\log_2$ fold change threshold of 0.25 and adjusted p-values (Padj) < 0.05 to define significance.

Fig. S2. Single-cell RNA sequencing of CD45$^+$ cells from the peritoneal cavity of ΔdblGATA mice versus WT controls. A) Top differentially expressed genes (DEGs) distinguishing large peritoneal macrophages (LPM) and small peritoneal macrophages (SPM). **B)** Signature scores based on expression of LPM markers (*Adgre1*, *Itgam*, *Gata6*, *Klf2*, *Mertk*, *Timd4*) and SPM markers (*Itgax*, *H2-Ab1*, *Ccr2*). **C)** UMAP visualization of LPM, SPM, and monocyte populations with clustering annotation. **D)** Identification of top differentially regulated transcription factors (TFs) in LPM, SPM, and monocyte populations between ΔdblGATA and WT mice. **E)** KEGG pathway enrichment analysis highlighting significantly activated pathways in LPM, SPM, and monocyte populations of ΔdblGATA mice compared to WT controls. **F)** UMAP visualization of LPM and SPM with clustering annotation. **G)** Identification of top differentially regulated TFs in LPM and SPM between ΔdblGATA and WT mice. **H)** KEGG pathway enrichment analysis highlighting significantly activated pathways in LPM and SPM of ΔdblGATA mice compared to WT controls. Statistical analysis of scRNAseq was performed using a $\log_2$ fold change threshold of 0.25 and adjusted p-values (Padj) < 0.05 to define significance.

Fig. S3. Transcriptional profiling of macrophages stimulated with EPX versus LPS at 8 and 24 hours. A) Principal component analysis (PCA) of bone marrow-derived macrophages (BMDMs) stimulated with 0.1 µg/mL EPX or 1 µg/mL LPS for 8 or 24 hours as compared to control condition (n = 4). **B)** Volcano plot highlighting differentially expressed genes (DEGs) between the 8-hour EPX-treated group and the 8-hour LPS-treated group. **C)** Volcano plot comparing DEGs in the 24-hour EPX-treated group versus the 24-hour LPS-treated group. **D)** Heatmap displaying the expression of key classical macrophage-associated genes in BMDMs following 8 or 24 hours of control, LPS, or EPX treatment. **E)** Heatmap displaying the expression of key alternatively activated macrophage-associated genes in BMDMs following 8 or 24 hours of control, LPS, or EPX treatment. **F)** Gene Ontology (GO) enrichment analysis of DEGs in the 8-hour EPX-treated group relative to the 8-hour LPS-treated group. Differential expression analysis was performed using a $\log_2$ fold change threshold of 1.0. P-values were adjusted using the Benjamini–Hochberg method to control the false discovery rate (FDR).

Genes with an adjusted P-value (Padj) < 0.05 were considered significantly differentially expressed.

Fig. S4. Transcriptional profiling of macrophages stimulated with EPX versus IL-4 at 8 and 24 hours. A) Principal component analysis (PCA) of bone marrow-derived macrophages (BMDMs) stimulated with 0.1 µg/mL EPX or 0.1 µg/mL IL-4 for 8 or 24 hours as compared to control condition (n = 4). **B)** Volcano plot highlighting differentially expressed genes (DEGs) between the 8-hour EPX-treated group and the 8-hour IL-4-treated group. **C)** Volcano plot comparing DEGs in the 24-hour EPX-treated group versus the 24-hour IL-4-treated group. **D)** Heatmap displaying the expression of key classical macrophage-associated genes in BMDMs following 8 or 24 hours of control, IL-4, or EPX treatment. **E)** Heatmap displaying the expression of key alternatively activated macrophage-associated genes in BMDMs following 8 or 24 hours of control, IL-4, or EPX treatment. **F)** Gene Ontology (GO) enrichment analysis of DEGs in the 24-hour EPX-treated group compared to the 24-hour IL-4-treated group. Differential expression analysis was performed using a $\log_2$ fold change threshold of 1.0. P-values were adjusted using the Benjamini–Hochberg method to control the false discovery rate (FDR). Genes with an adjusted P-value (Padj) < 0.05 were considered significantly differentially expressed.

Fig. S5. EPX attenuates LPS/IFN-γ–driven inflammatory activation in macrophages. BMDMs were stimulated for 24 hours with 1 µg/mL LPS and 0.1 µg/mL IFN-γ, in the presence or absence of 0.1 µg/mL EPX, compared to unstimulated controls. **A)** mRNA expression levels of *Acod1*, *Nos2*, and *Il10* (n = 3). **B)** Quantification of mean fluorescence intensity (MFI) for classical macrophage markers MHC-II and CD86 (n = 3). **C)** Oxygen consumption rate (OCR) profiles (n = 5). **D)** Quantification of key mitochondrial respiration parameters: basal respiration, maximal respiration, and ATP production (n = 5). **E)** Levels of pro-inflammatory cytokines TNFα and IL-1β in BMDM supernatants (n = 3). **F)** Levels of AAM-associated cytokines CCL22, CCL17, and IL-10 in BMDM supernatants (n = 3). Data are presented as mean ± SEM. Statistical significance was determined by one-way ANOVA followed by Tukey's multiple comparisons test. Asterisks indicate statistical significance: *p < 0.05, **p < 0.01, ***p < 0.001, ****p < 0.0001.

Fig. S6. Intranasal EPX administration reduced inflammation in LPS-induced acute lung injury. A) Schematic representation of the 40 µg LPS-induced acute lung injury model, established via intranasal (i.n.) administration on day 0, with or without concurrent i.n. treatment of 10 µg EPX on days 0 and 2 (n = 3–6). **B)** Quantification of lung injury scores based on histopathological assessment and **C)** representative hematoxylin and eosin (H&E) staining of lung tissue sections from control, LPS-challenged, and LPS+EPX-treated WT mice (n = 3–6). Scale bar: 100 µm. **D)** Gating strategy for spectral flow cytometry to identify key immune cell populations in the lungs: Neutrophils ($CD11b^+Ly6G^+$), Eosinophils ($CD11c^-SiglecF^+$), Patrolling monocytes ($MerTK^-CD11b^+Ly6C^{low}$), Inflammatory monocytes ($MerTK^-CD11b^+Ly6C^{high}$), Interstitial macrophages (IM; $CD11c^-SiglecF^-CD11b^+MerTK^+$), Classically activated IM ($CD11c^-SiglecF^-CD11b^+MerTK^+MHC\text{-}II^+CD206^-$), Alternatively activated IM ($CD11c^-SiglecF^-CD11b^+MerTK^+MHC\text{-}II^-CD206^+$), Alveolar macrophages (AM; $CD11c^+SiglecF^+MerTK^+$). **E)** Proportions of the identified immune cell populations in the lungs of control, LPS-challenged, and LPS+EPX-treated WT mice (n = 3–6). Data are presented as

mean ± SEM. Statistical significance was determined by one-way ANOVA followed by Tukey's multiple comparisons test. Asterisks indicate statistical significance: *p < 0.05, **p < 0.01, ***p < 0.001.

Supplementary Movie Legends

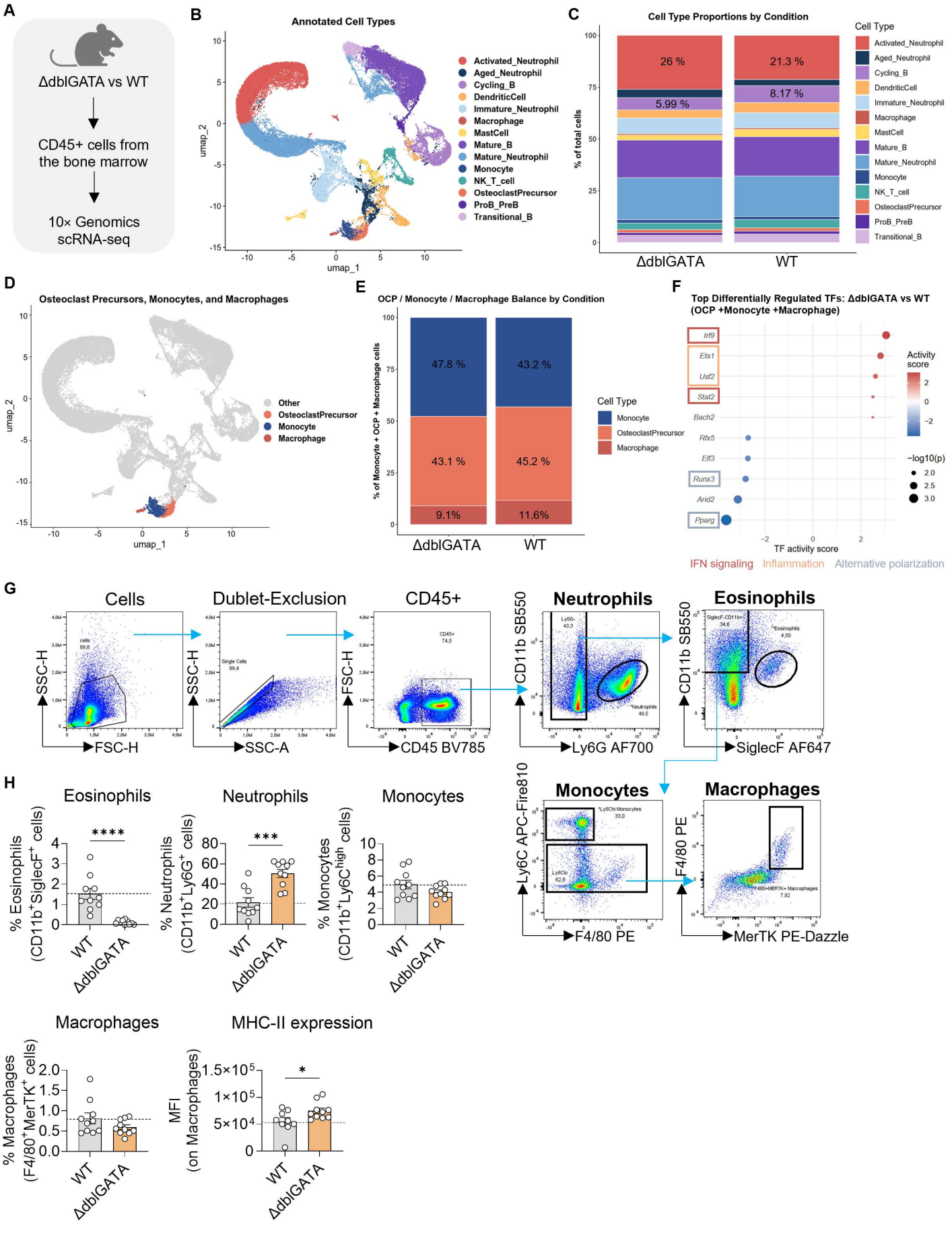
Movie S1. Live-cell imaging of apoptotic neutrophil engulfment by control macrophages. 24 hours after stimulation under control conditions, Cx3cr1-Cre;R26-tdTomato BMDMs (red) were incubated with CFSE-labeled apoptotic neutrophils (green) and monitored for 24 hours by live-cell imaging using a Zeiss spinning-disk Axio Observer Z1 microscope with a 63× objective, maintained at 37 °C and 5% CO_2. Scale bar: 15 µm.

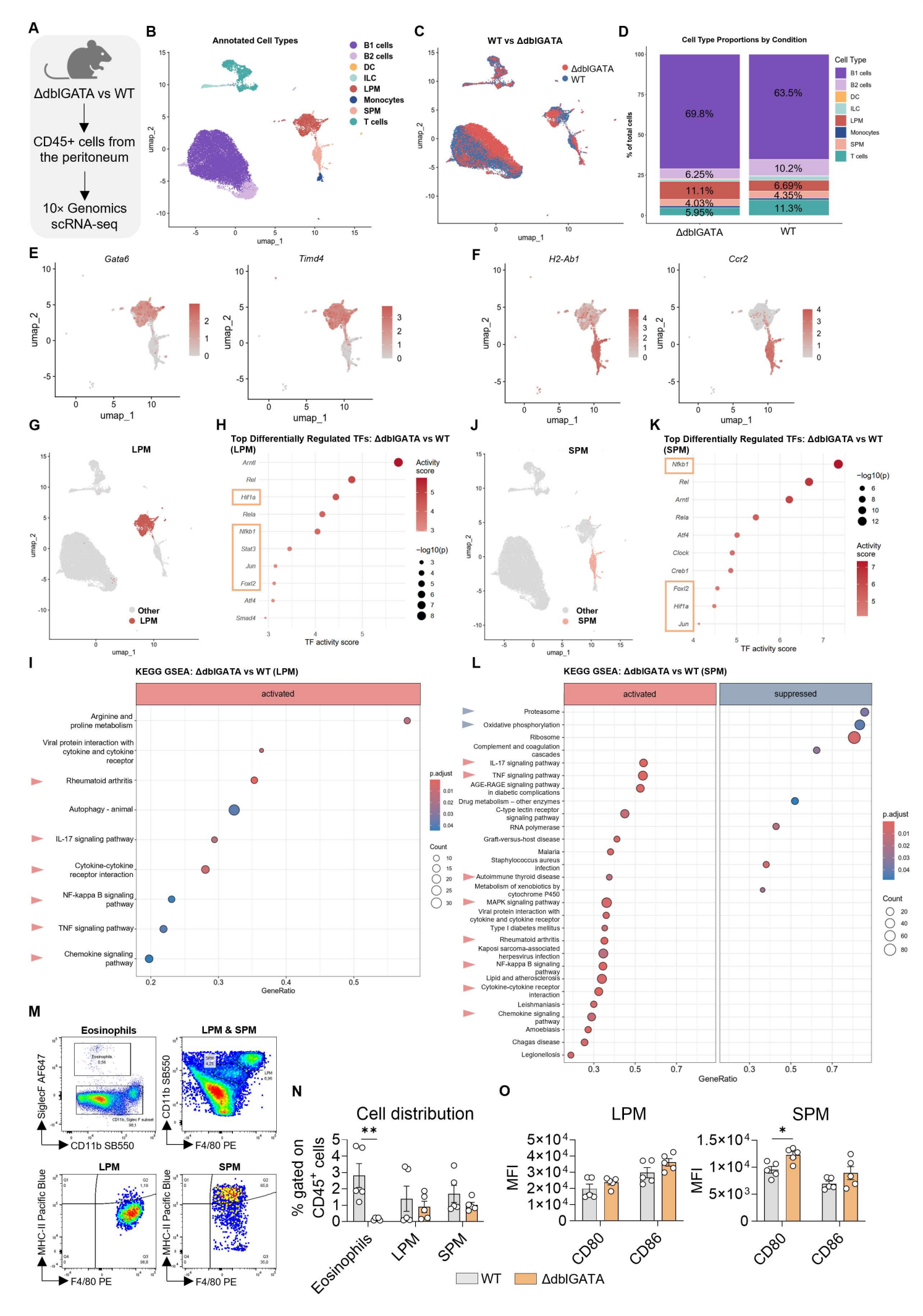
Movie S2. Live-cell imaging of apoptotic neutrophil engulfment by LPS-stimulated macrophages. 24 hours after stimulation with 1 µg/mL LPS, Cx3cr1-Cre;R26-tdTomato BMDMs (red) were incubated with CFSE-labeled apoptotic neutrophils (green) and monitored for 24 hours by live-cell imaging using a Zeiss spinning-disk Axio Observer Z1 microscope with a 63× objective, maintained at 37 °C and 5% CO_2. Scale bar: 15 µm.

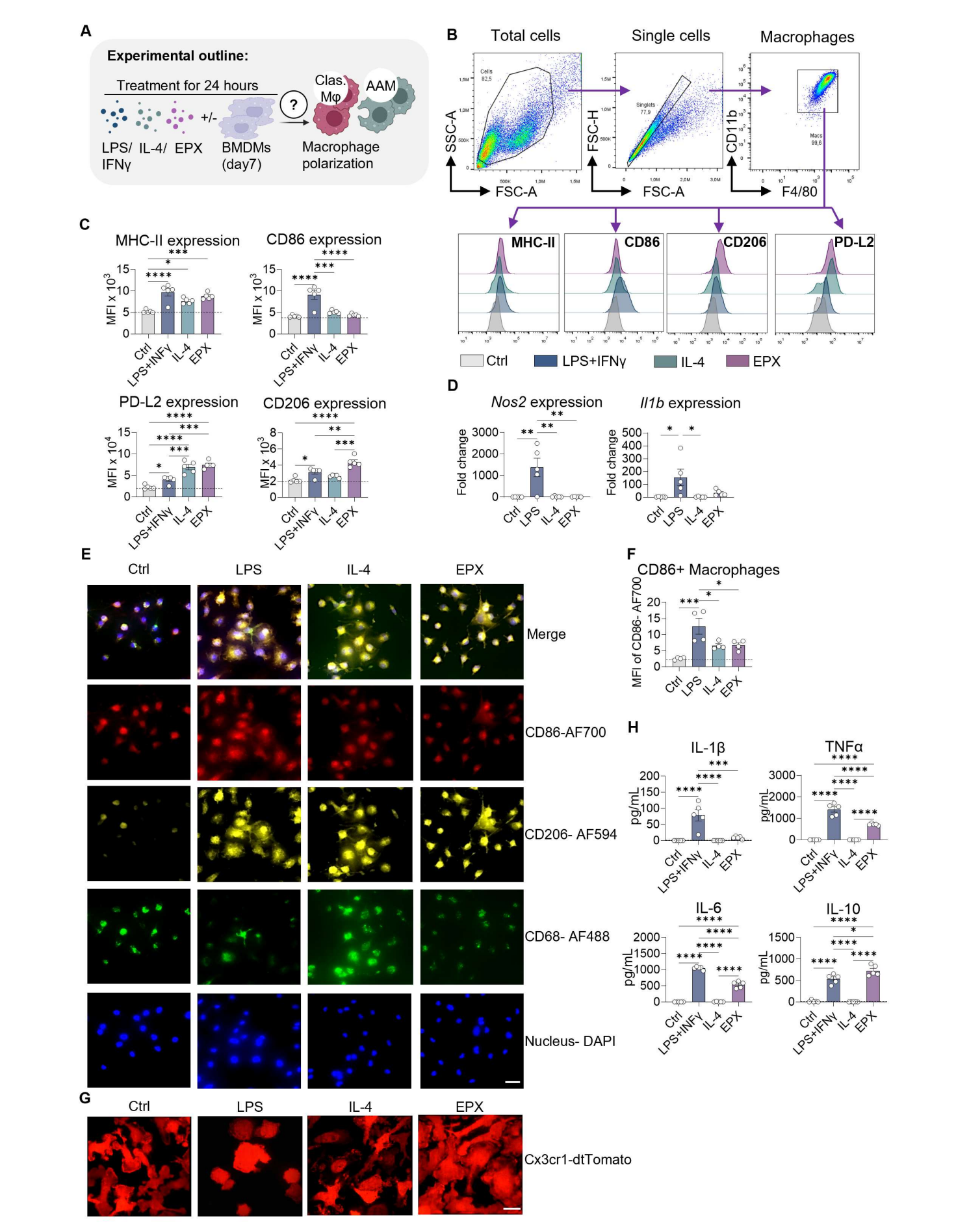
Movie S3. Live-cell imaging of apoptotic neutrophil engulfment by IL-4-stimulated macrophages. 24 hours after stimulation with 0.1 µg/mL IL-4, Cx3cr1-Cre;R26-tdTomato BMDMs (red) were incubated with CFSE-labeled apoptotic neutrophils (green) and monitored for 24 hours by live-cell imaging using a Zeiss spinning-disk Axio Observer Z1 microscope with a 63× objective, maintained at 37 °C and 5% CO_2. Scale bar: 15 µm.

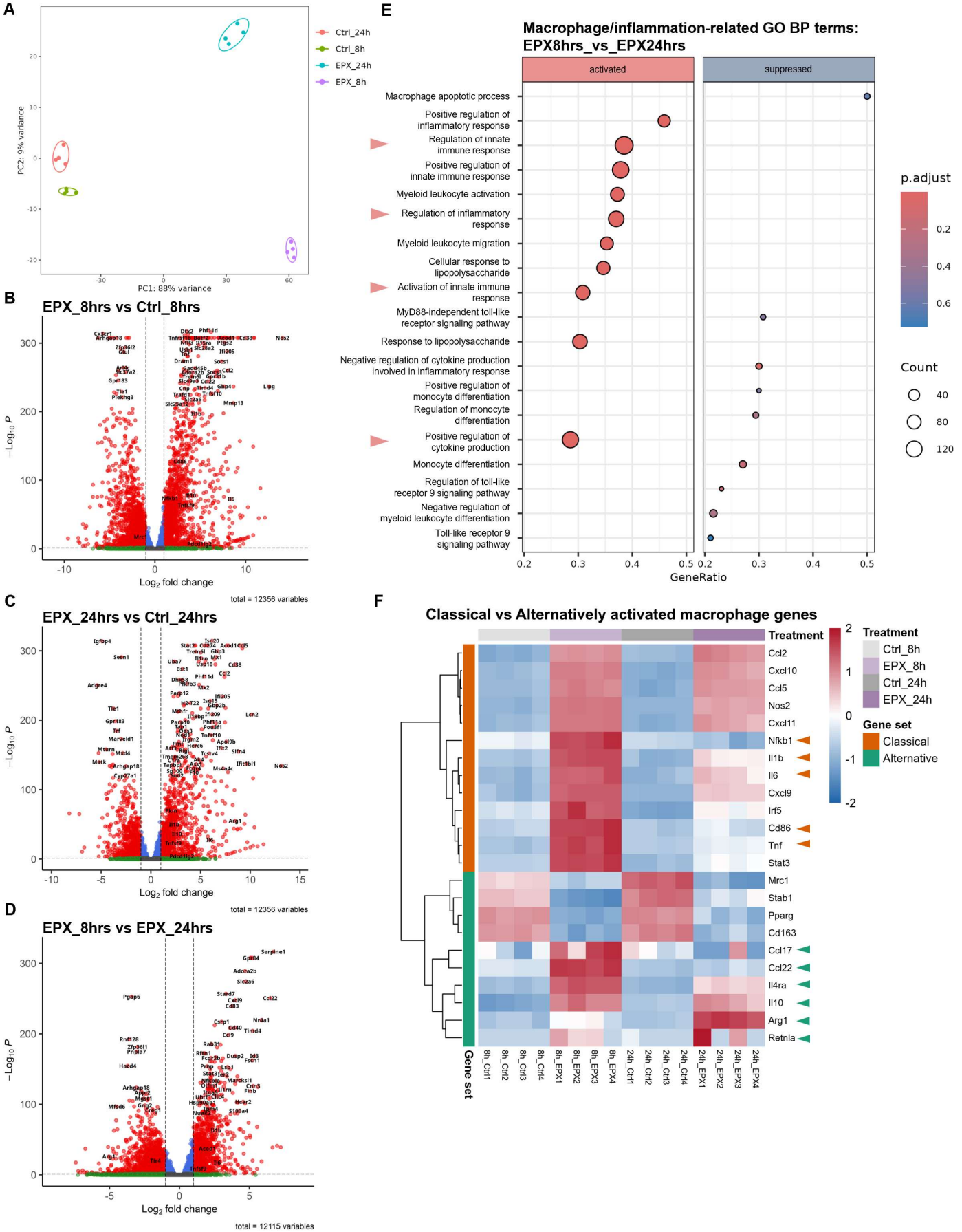
Movie S4. Live-cell imaging of apoptotic neutrophil engulfment by EPX-stimulated macrophages. 24 hours after stimulation with 0.1 µg/mL EPX, Cx3cr1-Cre;R26-tdTomato BMDMs (red) were incubated with CFSE-labeled apoptotic neutrophils (green) and monitored for 24 hours by live-cell imaging using a Zeiss spinning-disk Axio Observer Z1 microscope with a 63× objective, maintained at 37 °C and 5% CO_2. Scale bar: 15 µm.

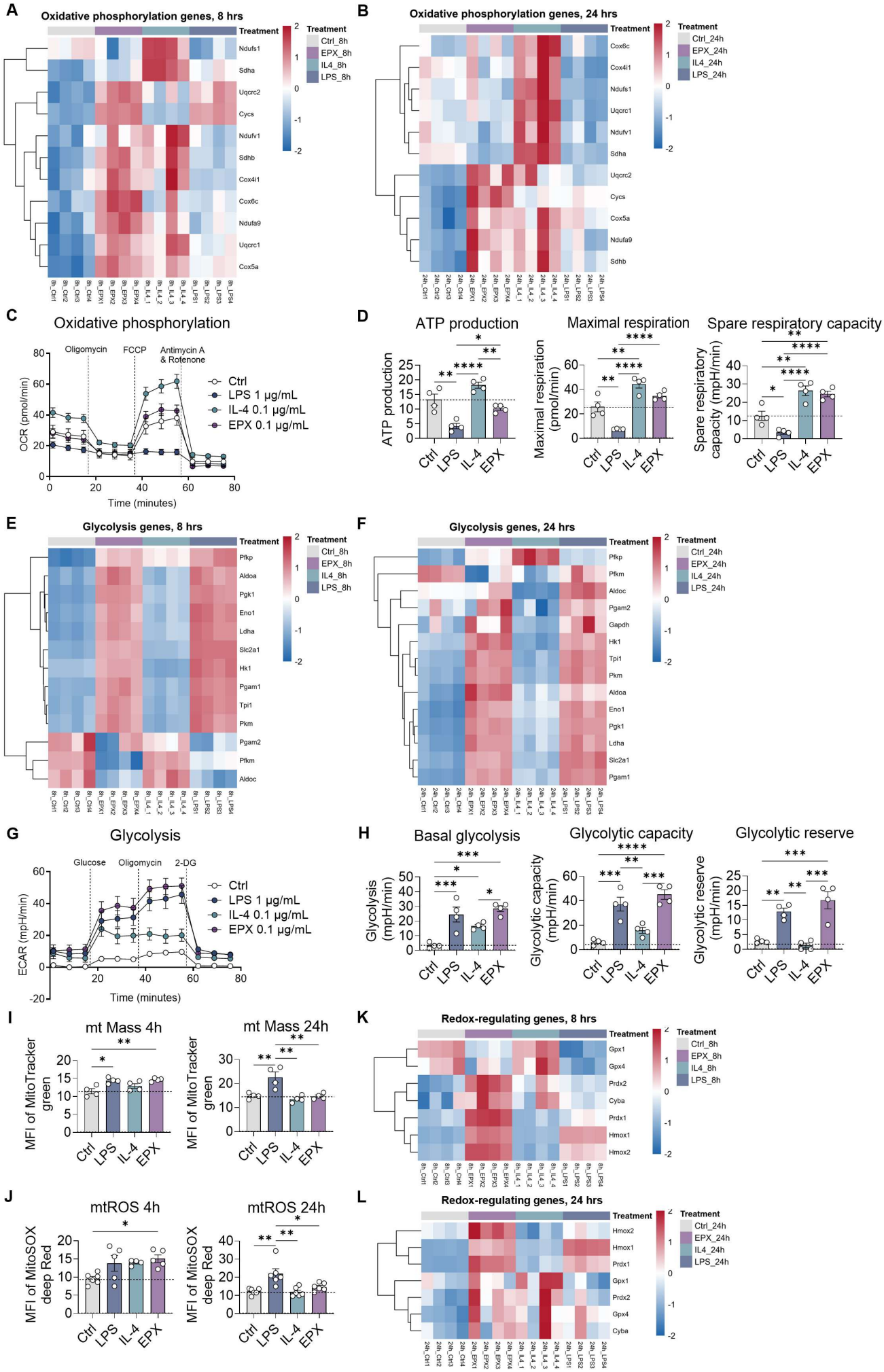
Movie S5. Z-stack acquisition showing internalization of EPX bound to CD11b. BMDMs were stimulated with Atto 647N-labeled EPX (red) for 24 hours, followed by fixation and staining with anti-CD11b Alexa Fluor 488 (green) and DAPI (blue). Images were acquired using a Leica Stellaris 8 confocal microscope with a 63× objective and Z-stack acquisition. Scale bar: 10 µm.

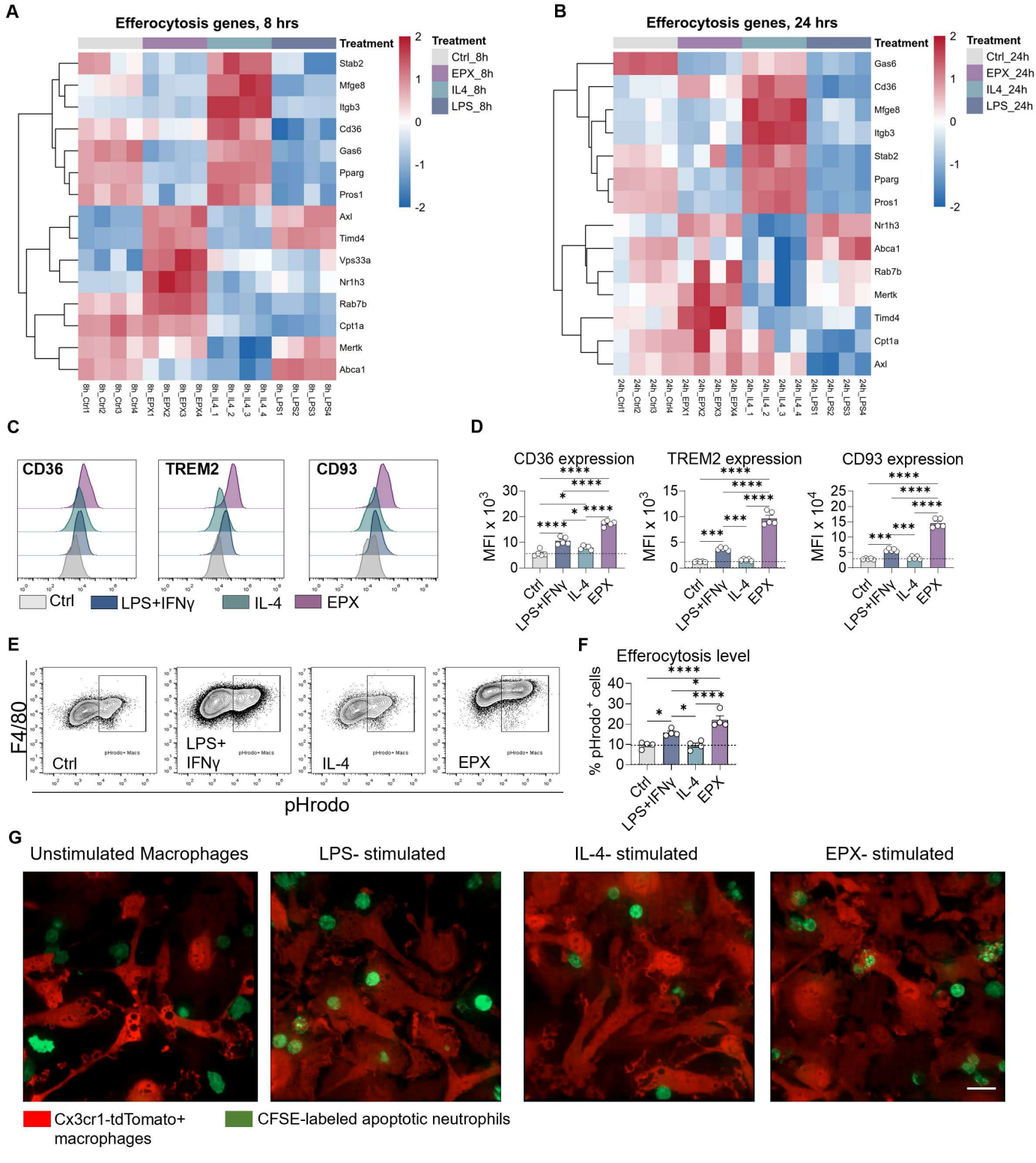

A
ΔdblGATA vs WT
CD45+ cells from the bone marrow
10× Genomics scRNA-seq
B
Annotated Cell Types
umap_1
umap_2
Activated_Neutrophil
Aged_Neutrophil
Cycling_B
DendriticCell
Immature_Neutrophil
Macrophage
MastCell
Mature_B
Mature_Neutrophil
Monocyte
NK_T_cell
OsteoclastPrecursor
ProB_PreB
Transitional_B
C
Cell Type Proportions by Condition
% of total cells
26 %
21.3 %
5.99 %
8.17 %
ΔdblGATA
WT
Cell Type
D
Osteoclast Precursors, Monocytes, and Macrophages
umap_1
umap_2
Other
OsteoclastPrecursor
Monocyte
Macrophage
E
OCP / Monocyte / Macrophage Balance by Condition
% of Monocyte + OCP + Macrophage cells
47.8 %
43.2 %
43.1 %
45.2 %
9.1%
11.6%
ΔdblGATA
WT
Cell Type
Monocyte
OsteoclastPrecursor
Macrophage
F
Top Differentially Regulated TFs: ΔdblGATA vs WT
(OCP +Monocyte +Macrophage)
Irf9
Ets1
Usf2
Stat2
Bach2
Rfx5
Elf3
Runx3
Arid2
Pparg
Activity score
−log10(p)
TF activity score
IFN signaling
Inflammation
Alternative polarization
G
Cells
Dublet-Exclusion
CD45+
Neutrophils
Eosinophils
SSC-H
FSC-H
SSC-A
CD45 BV785
CD11b SB550
Ly6G AF700
SiglecF AF647
H
Eosinophils
Neutrophils
Monocytes
% Eosinophils (CD11b+SiglecF+ cells)
% Neutrophils (CD11b+Ly6G+ cells)
% Monocytes (CD11b+Ly6Chigh cells)
****
***
WT
ΔdblGATA
Monocytes
Macrophages
Ly6C APC-Fire810
F4/80 PE
MerTK PE-Dazzle
Macrophages
MHC-II expression
% Macrophages (F4/80+MerTK+ cells)
MFI (on Macrophages)
*

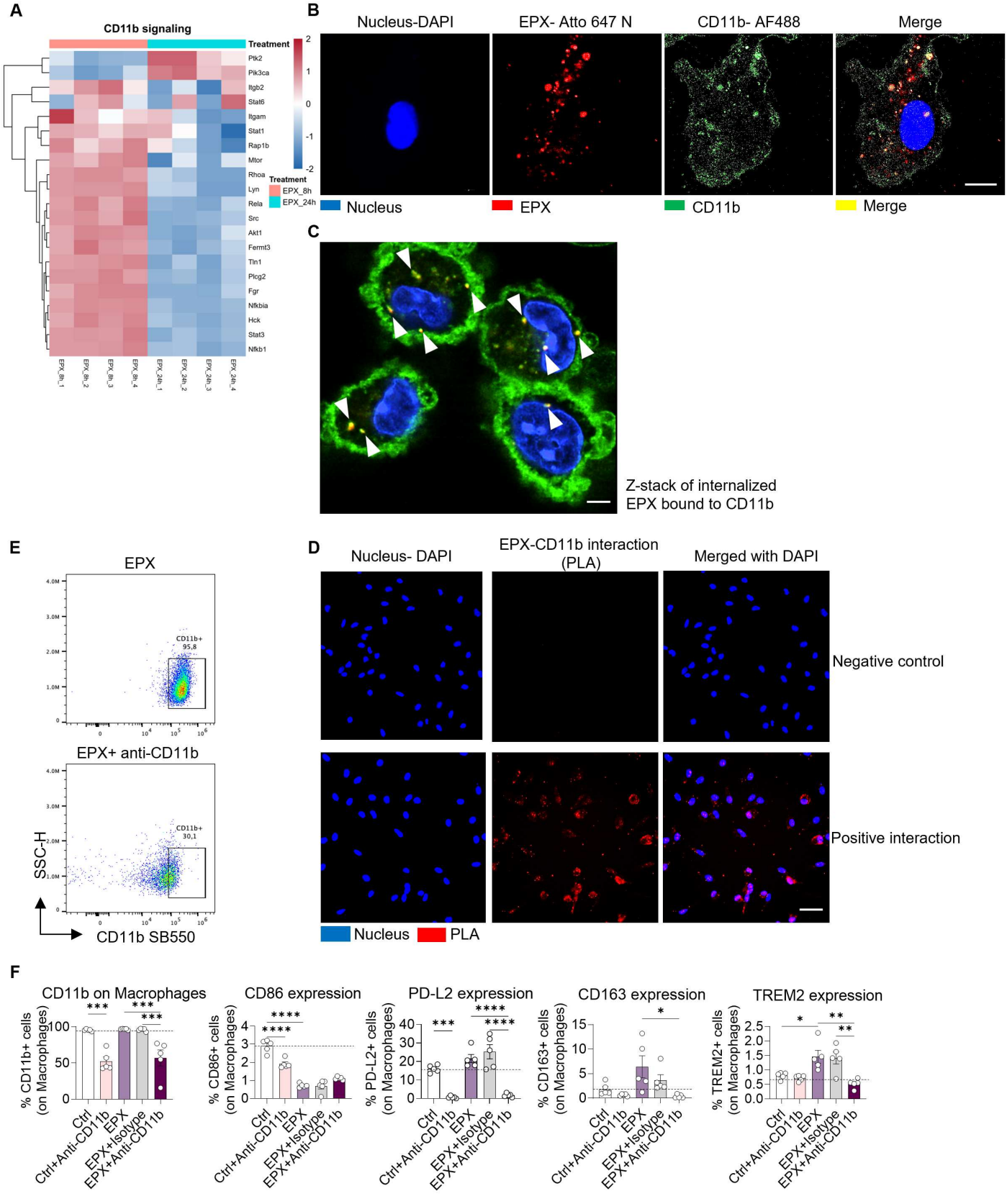

A
ΔdblGATA vs WT
CD45+ cells from the peritoneum
10× Genomics scRNA-seq
B
Annotated Cell Types
B1 cells
B2 cells
DC
ILC
LPM
Monocytes
SPM
T cells
umap_1
umap_2
C
WT vs ΔdblGATA
ΔdblGATA
WT
D
Cell Type Proportions by Condition
% of total cells
69.8%
6.25%
11.1%
4.03%
5.95%
63.5%
10.2%
6.69%
4.35%
11.3%
ΔdblGATA
WT
E
Gata6
Timd4
F
H2-Ab1
Ccr2
G
LPM
Other
LPM
H
Top Differentially Regulated TFs: ΔdblGATA vs WT (LPM)
Arntl
Rel
Hif1a
Rela
Nfkb1
Stat3
Jun
Foxl2
Atf4
Smad4
Activity score
−log10(p)
TF activity score
J
SPM
Other
SPM
K
Top Differentially Regulated TFs: ΔdblGATA vs WT (SPM)
Nfkb1
Rel
Arntl
Rela
Atf4
Clock
Creb1
Foxl2
Hif1a
Jun
I
KEGG GSEA: ΔdblGATA vs WT (LPM)
activated
Arginine and proline metabolism
Viral protein interaction with cytokine and cytokine receptor
Rheumatoid arthritis
Autophagy - animal
IL-17 signaling pathway
Cytokine-cytokine receptor interaction
NF-kappa B signaling pathway
TNF signaling pathway
Chemokine signaling pathway
p.adjust
Count
GeneRatio
L
KEGG GSEA: ΔdblGATA vs WT (SPM)
activated
suppressed
Proteasome
Oxidative phosphorylation
Ribosome
Complement and coagulation cascades
IL-17 signaling pathway
TNF signaling pathway
AGE-RAGE signaling pathway in diabetic complications
Drug metabolism – other enzymes
C-type lectin receptor signaling pathway
RNA polymerase
Graft-versus-host disease
Malaria
Staphylococcus aureus infection
Autoimmune thyroid disease
Metabolism of xenobiotics by cytochrome P450
MAPK signaling pathway
Viral protein interaction with cytokine and cytokine receptor
Type I diabetes mellitus
Rheumatoid arthritis
Kaposi sarcoma-associated herpesvirus infection
NF-kappa B signaling pathway
Lipid and atherosclerosis
Cytokine-cytokine receptor interaction
Leishmaniasis
Chemokine signaling pathway
Amoebiasis
Chagas disease
Legionellosis
p.adjust
Count
GeneRatio
M
Eosinophils
LPM & SPM
SiglecF AF647
CD11b SB550
CD11b SB550
F4/80 PE
LPM
SPM
MHC-II Pacific Blue
F4/80 PE
MHC-II Pacific Blue
F4/80 PE
N
Cell distribution
% gated on CD45+ cells
**
Eosinophils
LPM
SPM
O
LPM
SPM
MFI
*
CD80
CD86
CD80
CD86
WT
ΔdblGATA

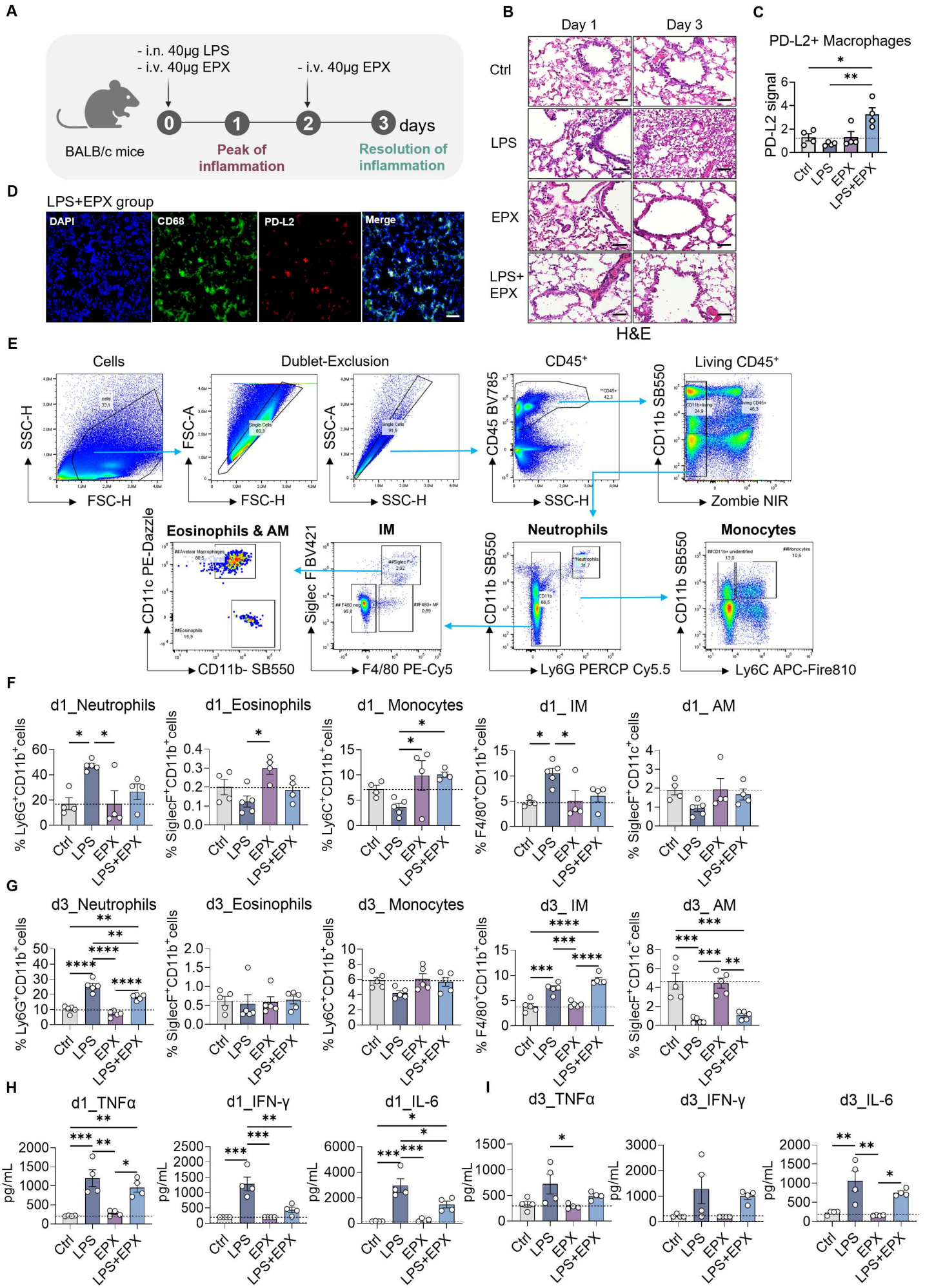

A
Experimental outline:
Treatment for 24 hours
LPS/ IFNγ
IL-4/ EPX
+/-
BMDMs (day7)
?
Clas. Mφ
AAM
Macrophage polarization
B
Total cells
Single cells
Macrophages
SSC-A
FSC-A
FSC-H
CD11b
F4/80
MHC-II
CD86
CD206
PD-L2
Ctrl
LPS+IFNγ
IL-4
EPX
C
MHC-II expression
CD86 expression
PD-L2 expression
CD206 expression
MFI x 10^3
MFI x 10^4
D
Nos2 expression
Il1b expression
Fold change
E
Merge
CD86-AF700
CD206- AF594
CD68- AF488
Nucleus- DAPI
F
CD86+ Macrophages
MFI of CD86- AF700
H
IL-1β
TNFα
IL-6
IL-10
pg/mL
G
Cx3cr1-dtTomato

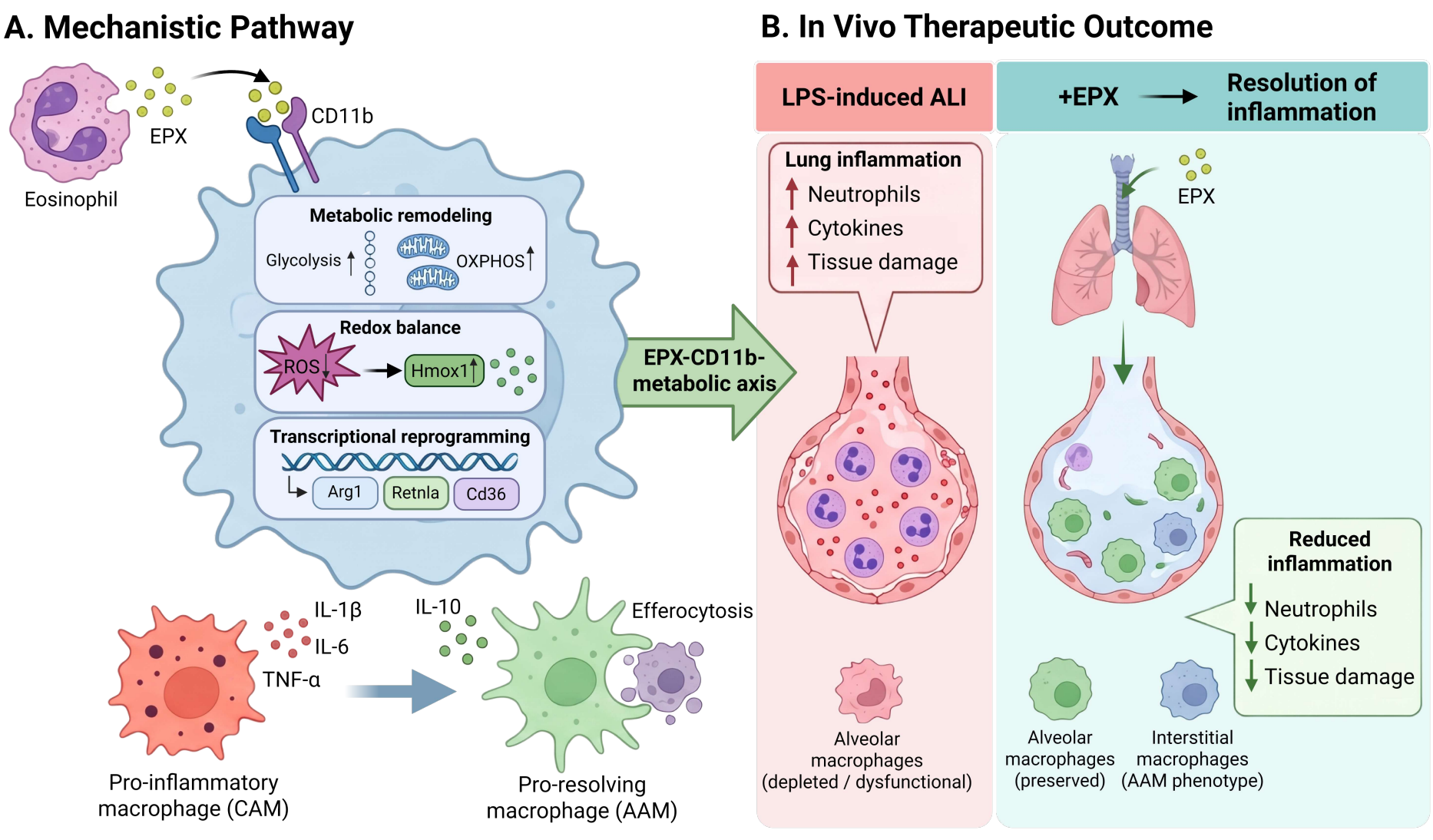

A
Ctrl_24h
Ctrl_8h
EPX_24h
EPX_8h
PC2: 9% variance
PC1: 88% variance
B
EPX_8hrs vs Ctrl_8hrs
−Log10 P
Log2 fold change
C
EPX_24hrs vs Ctrl_24hrs
total = 12356 variables
−Log10 P
Log2 fold change
D
EPX_8hrs vs EPX_24hrs
total = 12356 variables
total = 12115 variables
−Log10 P
Log2 fold change
E
Macrophage/inflammation-related GO BP terms:
EPX8hrs_vs_EPX24hrs
activated
suppressed
Macrophage apoptotic process
Positive regulation of inflammatory response
Regulation of innate immune response
Positive regulation of innate immune response
Myeloid leukocyte activation
Regulation of inflammatory response
Myeloid leukocyte migration
Cellular response to lipopolysaccharide
Activation of innate immune response
MyD88-independent toll-like receptor signaling pathway
Response to lipopolysaccharide
Negative regulation of cytokine production involved in inflammatory response
Positive regulation of monocyte differentiation
Regulation of monocyte differentiation
Positive regulation of cytokine production
Monocyte differentiation
Regulation of toll-like receptor 9 signaling pathway
Negative regulation of myeloid leukocyte differentiation
Toll-like receptor 9 signaling pathway
GeneRatio
p.adjust
Count
F
Classical vs Alternatively activated macrophage genes
Treatment
Ctrl_8h
EPX_8h
Ctrl_24h
EPX_24h
Gene set
Classical
Alternative
Ccl2
Cxcl10
Ccl5
Nos2
Cxcl11
Nfkb1
Il1b
Il6
Cxcl9
Irf5
Cd86
Tnf
Stat3
Mrc1
Stab1
Pparg
Cd163
Ccl17
Ccl22
Il4ra
Il10
Arg1
Retnla
8h_Ctrl1
8h_Ctrl2
8h_Ctrl3
8h_Ctrl4
8h_EPX1
8h_EPX2
8h_EPX3
8h_EPX4
24h_Ctrl1
24h_Ctrl2
24h_Ctrl3
24h_Ctrl4
24h_EPX1
24h_EPX2
24h_EPX3
24h_EPX4
Gene set

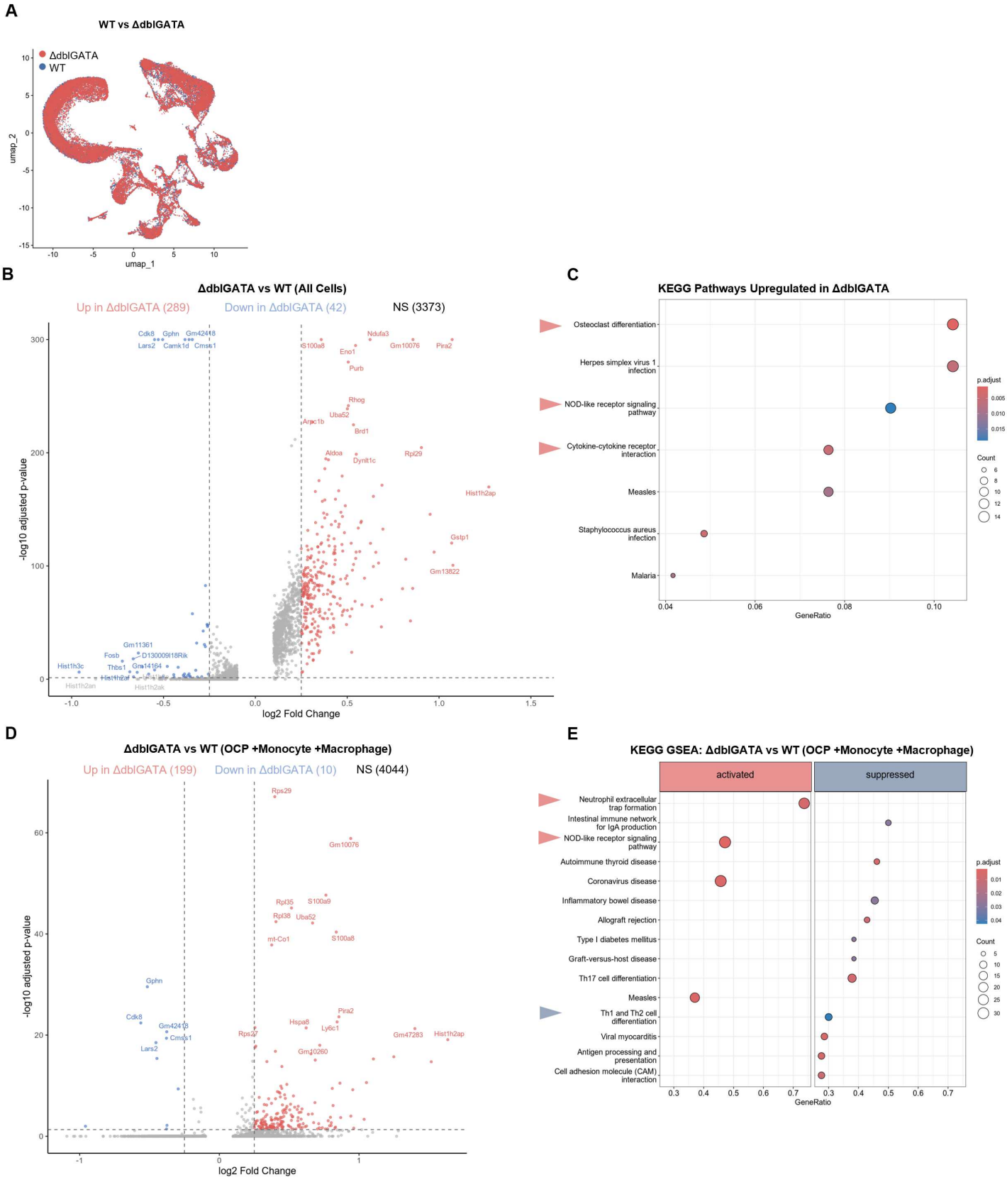

A
Oxidative phosphorylation genes, 8 hrs
Treatment
Ctrl_8h
EPX_8h
IL4_8h
LPS_8h
Ndufs1
Sdha
Uqcrc2
Cycs
Ndufv1
Sdhb
Cox4i1
Cox6c
Ndufa9
Uqcrc1
Cox5a
B
Oxidative phosphorylation genes, 24 hrs
Ctrl_24h
EPX_24h
IL4_24h
LPS_24h
Cox6c
Cox4i1
Ndufs1
Uqcrc1
Ndufv1
Sdha
Uqcrc2
Cycs
Cox5a
Ndufa9
Sdhb
C
Oxidative phosphorylation
Oligomycin
FCCP
Antimycin A & Rotenone
OCR (pmol/min)
Time (minutes)
Ctrl
LPS 1 µg/mL
IL-4 0.1 µg/mL
EPX 0.1 µg/mL
D
ATP production
Maximal respiration
Spare respiratory capacity
ATP production
Maximal respiration (pmol/min)
Spare respiratory capacity (mpH/min)
Ctrl
LPS
IL-4
EPX
E
Glycolysis genes, 8 hrs
Pfkp
Aldoa
Pgk1
Eno1
Ldha
Slc2a1
Hk1
Pgam1
Tpi1
Pkm
Pgam2
Pfkm
Aldoc
F
Glycolysis genes, 24 hrs
Pfkp
Pfkm
Aldoc
Pgam2
Gapdh
Hk1
Tpi1
Pkm
Aldoa
Eno1
Pgk1
Ldha
Slc2a1
Pgam1
G
Glycolysis
Glucose
Oligomycin
2-DG
ECAR (mpH/min)
Time (minutes)
H
Basal glycolysis
Glycolytic capacity
Glycolytic reserve
Glycolysis (mpH/min)
Glycolytic capacity (mpH/min)
Glycolytic reserve (mpH/min)
I
mt Mass 4h
mt Mass 24h
MFI of MitoTracker green
J
mtROS 4h
mtROS 24h
MFI of MitoSOX deep Red
K
Redox-regulating genes, 8 hrs
Gpx1
Gpx4
Prdx2
Cyba
Prdx1
Hmox1
Hmox2
L
Redox-regulating genes, 24 hrs
Hmox2
Hmox1
Prdx1
Gpx1
Prdx2
Gpx4
Cyba

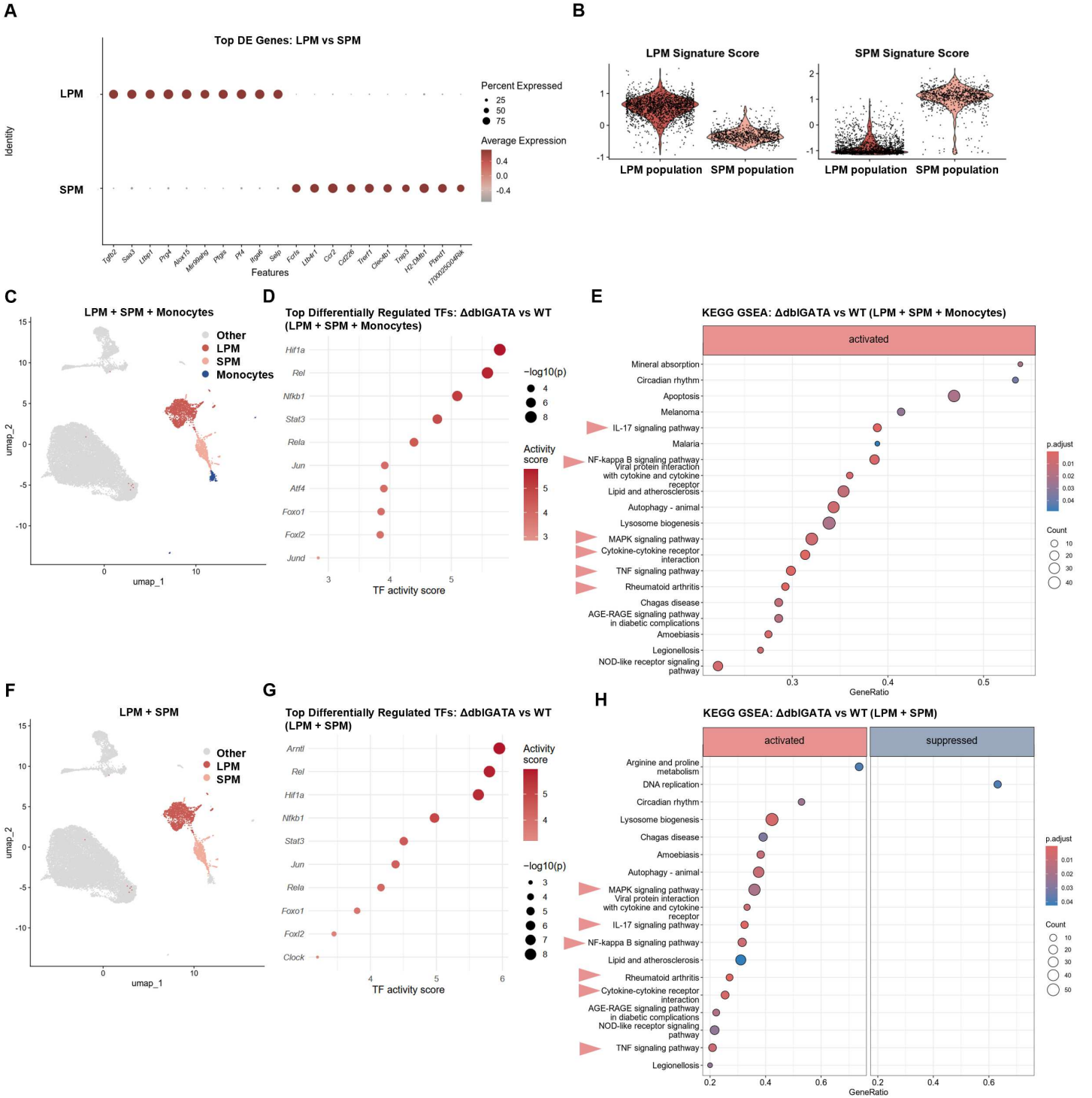

A
Efferocytosis genes, 8 hrs
Treatment
Ctrl_8h
EPX_8h
IL4_8h
LPS_8h
Stab2
Mfge8
Itgb3
Cd36
Gas6
Pparg
Pros1
Axl
Timd4
Vps33a
Nr1h3
Rab7b
Cpt1a
Mertk
Abca1
B
Efferocytosis genes, 24 hrs
Ctrl_24h
EPX_24h
IL4_24h
LPS_24h
C
CD36
TREM2
CD93
Ctrl
LPS+IFNγ
IL-4
EPX
D
CD36 expression
TREM2 expression
CD93 expression
MFI x 10^3
MFI x 10^4
E
F4/80
pHrodo
LPS+ IFNγ
F
Efferocytosis level
% pHrodo+ cells
G
Unstimulated Macrophages
LPS- stimulated
IL-4- stimulated
EPX- stimulated
Cx3cr1-tdTomato+ macrophages
CFSE-labeled apoptotic neutrophils

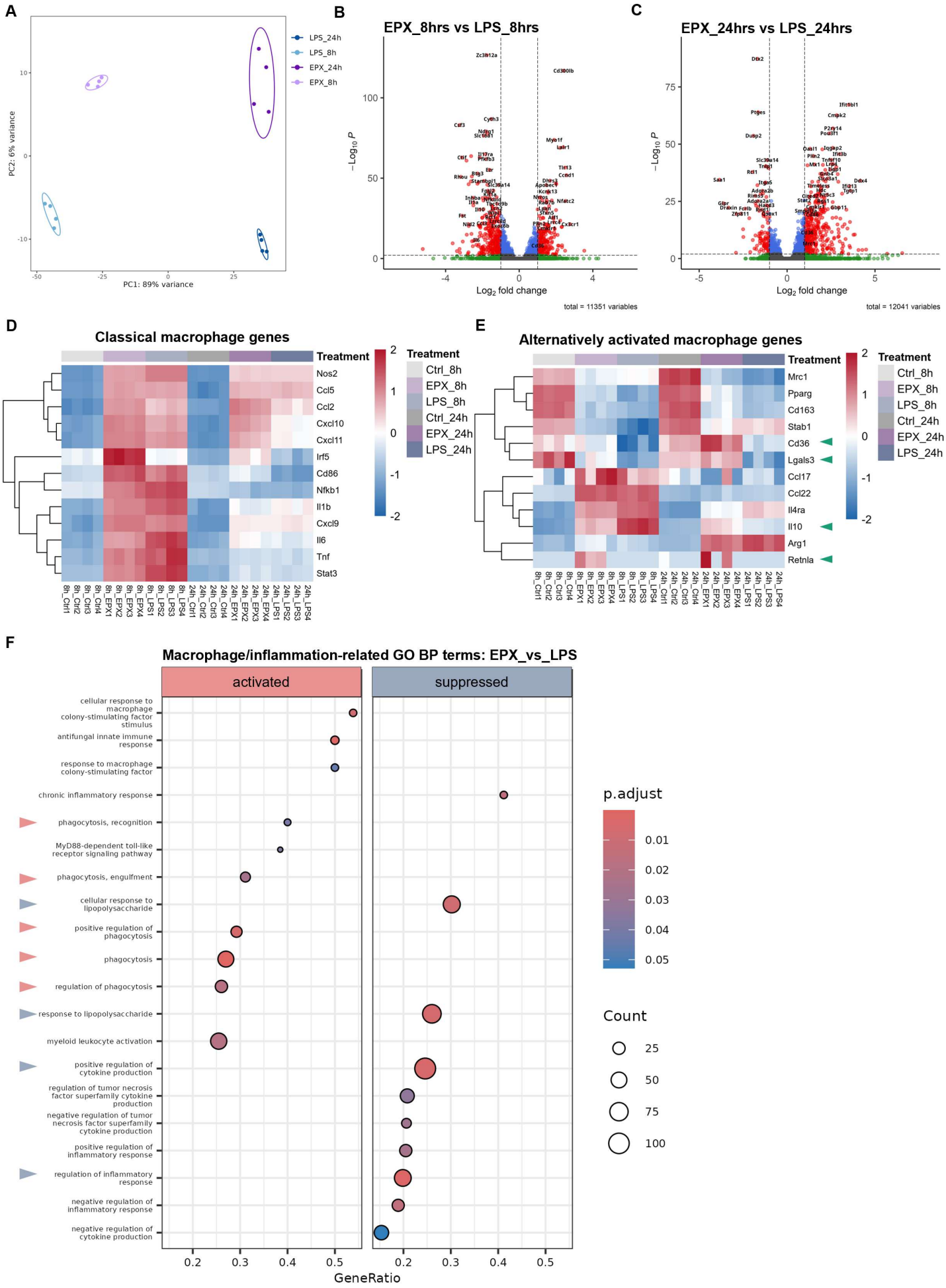

A
CD11b signaling
Treatment
Ptk2
Pik3ca
Itgb2
Stat6
Itgam
Stat1
Rap1b
Mtor
Rhoa
Lyn
Rela
Src
Akt1
Fermt3
Tln1
Plcg2
Fgr
Nfkbia
Hck
Stat3
Nfkb1
EPX_8h_1
EPX_8h_2
EPX_8h_3
EPX_8h_4
EPX_24h_1
EPX_24h_2
EPX_24h_3
EPX_24h_4
Treatment
EPX_8h
EPX_24h
B
Nucleus-DAPI
EPX- Atto 647 N
CD11b- AF488
Merge
Nucleus
EPX
CD11b
Merge
C
Z-stack of internalized
EPX bound to CD11b
D
Nucleus- DAPI
EPX-CD11b interaction
(PLA)
Merged with DAPI
Negative control
Positive interaction
Nucleus
PLA
E
EPX
CD11b+
95,8
EPX+ anti-CD11b
CD11b+
30,1
SSC-H
CD11b SB550
F
CD11b on Macrophages
% CD11b+ cells
(on Macrophages)
CD86 expression
% CD86+ cells
(on Macrophages)
PD-L2 expression
% PD-L2+ cells
(on Macrophages)
CD163 expression
% CD163+ cells
(on Macrophages)
TREM2 expression
% TREM2+ cells
(on Macrophages)
Ctrl
Ctrl+Anti-CD11b
EPX
EPX+Isotype
EPX+Anti-CD11b

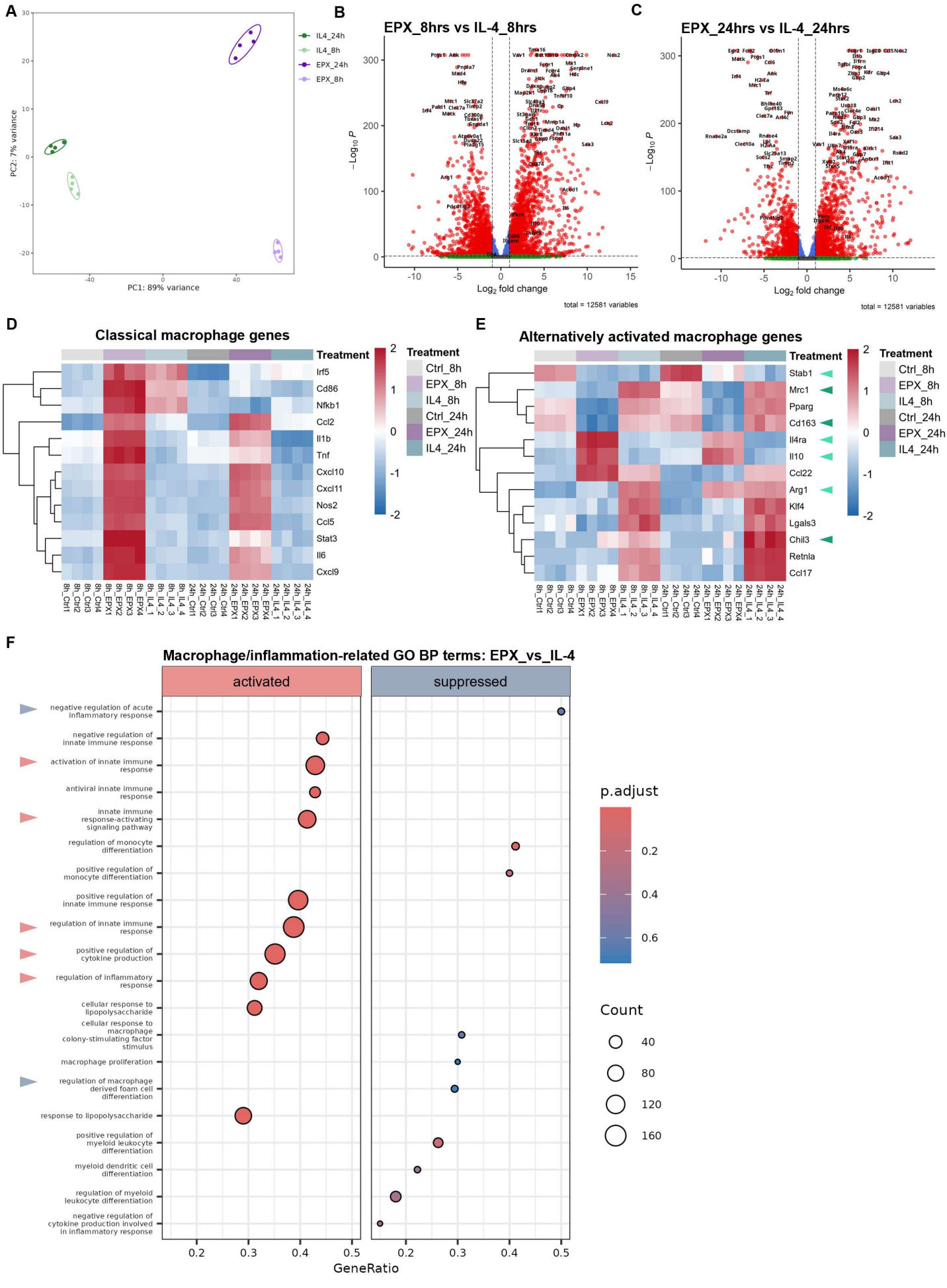

A
- i.n. 40µg LPS
- i.v. 40µg EPX
- i.v. 40µg EPX
0
1
2
3 days
BALB/c mice
Peak of inflammation
Resolution of inflammation
B
Day 1
Day 3
Ctrl
LPS
EPX
LPS+ EPX
H&E
C
PD-L2+ Macrophages
PD-L2 signal
Ctrl
LPS
EPX
LPS+EPX
D
LPS+EPX group
DAPI
CD68
PD-L2
Merge
E
Cells
Dublet-Exclusion
CD45+
Living CD45+
SSC-H
FSC-H
FSC-A
SSC-A
CD45 BV785
CD11b SB550
Zombie NIR
Eosinophils & AM
IM
Neutrophils
Monocytes
CD11c PE-Dazzle
CD11b- SB550
Siglec F BV421
F4/80 PE-Cy5
Ly6G PERCP Cy5.5
Ly6C APC-Fire810
F
d1_Neutrophils
d1_Eosinophils
d1_ Monocytes
d1_ IM
d1_ AM
% Ly6G+CD11b+cells
% SiglecF+CD11b+cells
% Ly6C+CD11b+cells
% F4/80+CD11b+cells
% SiglecF+CD11c+cells
G
d3_Neutrophils
d3_Eosinophils
d3_ Monocytes
d3_ IM
d3_ AM
H
d1_TNFα
d1_IFN-γ
d1_IL-6
pg/mL
I
d3_TNFα
d3_IFN-γ
d3_IL-6

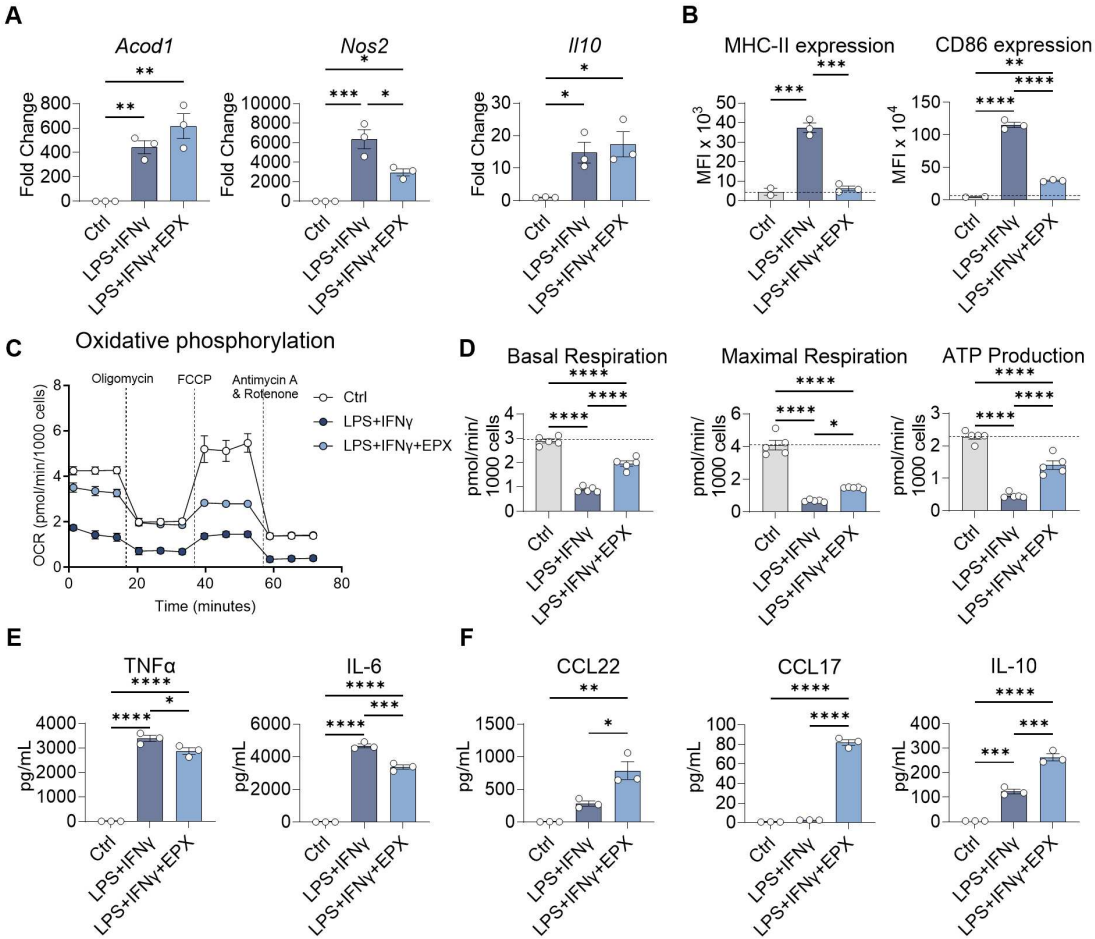

A. Mechanistic Pathway
B. In Vivo Therapeutic Outcome
Eosinophil
EPX
CD11b
Metabolic remodeling
Glycolysis
OXPHOS
Redox balance
ROS
Hmox1
Transcriptional reprogramming
Arg1
Retnla
Cd36
EPX-CD11b-metabolic axis
IL-1β
IL-6
TNF-α
Pro-inflammatory macrophage (CAM)
IL-10
Efferocytosis
Pro-resolving macrophage (AAM)
LPS-induced ALI
Lung inflammation
Neutrophils
Cytokines
Tissue damage
Alveolar macrophages (depleted / dysfunctional)
+EPX
Resolution of inflammation
EPX
Reduced inflammation
Neutrophils
Cytokines
Tissue damage
Alveolar macrophages (preserved)
Interstitial macrophages (AAM phenotype)

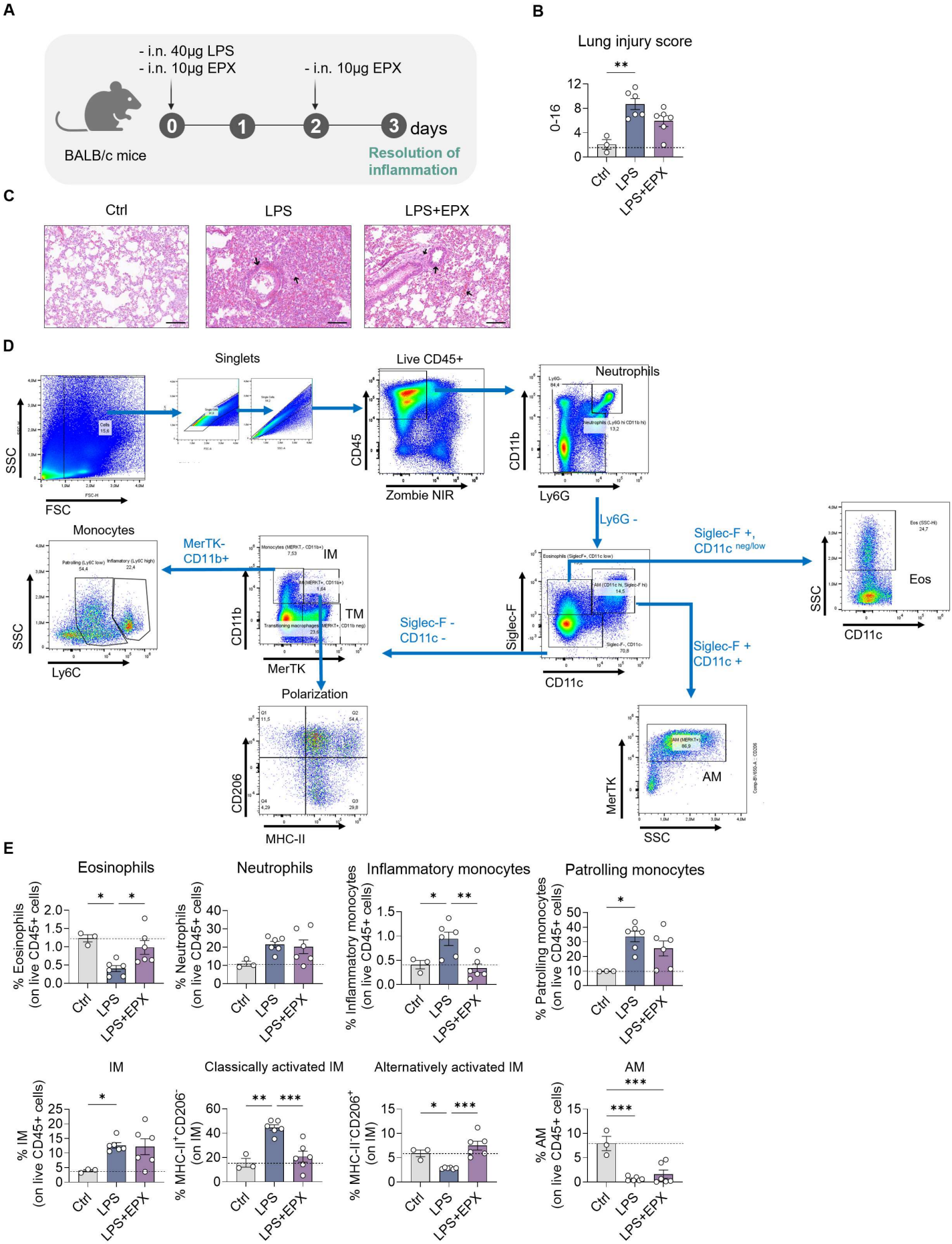

A
WT vs ΔdblGATA
ΔdblGATA
WT
umap_2
umap_1
B
ΔdblGATA vs WT (All Cells)
Up in ΔdblGATA (289)
Down in ΔdblGATA (42)
NS (3373)
-log10 adjusted p-value
log2 Fold Change
C
KEGG Pathways Upregulated in ΔdblGATA
Osteoclast differentiation
Herpes simplex virus 1 infection
NOD-like receptor signaling pathway
Cytokine-cytokine receptor interaction
Measles
Staphylococcus aureus infection
Malaria
GeneRatio
p.adjust
Count
D
ΔdblGATA vs WT (OCP +Monocyte +Macrophage)
Up in ΔdblGATA (199)
Down in ΔdblGATA (10)
NS (4044)
-log10 adjusted p-value
log2 Fold Change
E
KEGG GSEA: ΔdblGATA vs WT (OCP +Monocyte +Macrophage)
activated
suppressed
Neutrophil extracellular trap formation
Intestinal immune network for IgA production
NOD-like receptor signaling pathway
Autoimmune thyroid disease
Coronavirus disease
Inflammatory bowel disease
Allograft rejection
Type I diabetes mellitus
Graft-versus-host disease
Th17 cell differentiation
Measles
Th1 and Th2 cell differentiation
Viral myocarditis
Antigen processing and presentation
Cell adhesion molecule (CAM) interaction
GeneRatio
p.adjust
Count


A
Top DE Genes: LPM vs SPM
LPM
SPM
Identity
Percent Expressed
25
50
75
Average Expression
0.4
0.0
-0.4
Tgfb2
Saa3
Ltbp1
Ptgr4
Alox15
Mir99ahg
Ptgis
Pf4
Itga6
Selp
Fcrls
Ltbr1
Ccr2
Cd226
Trerf1
Clec4b1
Traj3
H2-DMb1
Phrf1
1700025G04Rik
Features
B
LPM Signature Score
SPM Signature Score
LPM population
SPM population
LPM population
SPM population
C
LPM + SPM + Monocytes
Other
LPM
SPM
Monocytes
umap_2
umap_1
D
Top Differentially Regulated TFs: ΔdbIGATA vs WT
(LPM + SPM + Monocytes)
Hif1a
Rel
Nfkb1
Stat3
Rela
Jun
Atf4
Foxo1
Foxl2
Jund
−log10(p)
Activity score
TF activity score
E
KEGG GSEA: ΔdbIGATA vs WT (LPM + SPM + Monocytes)
activated
Mineral absorption
Circadian rhythm
Apoptosis
Melanoma
IL-17 signaling pathway
Malaria
NF-kappa B signaling pathway
Viral protein interaction with cytokine and cytokine receptor
Lipid and atherosclerosis
Autophagy - animal
Lysosome biogenesis
MAPK signaling pathway
Cytokine-cytokine receptor interaction
TNF signaling pathway
Rheumatoid arthritis
Chagas disease
AGE-RAGE signaling pathway in diabetic complications
Amoebiasis
Legionellosis
NOD-like receptor signaling pathway
p.adjust
Count
GeneRatio
F
LPM + SPM
Other
LPM
SPM
umap_2
umap_1
G
Top Differentially Regulated TFs: ΔdbIGATA vs WT
(LPM + SPM)
Arntl
Rel
Hif1a
Nfkb1
Stat3
Jun
Rela
Foxo1
Foxl2
Clock
Activity score
−log10(p)
TF activity score
H
KEGG GSEA: ΔdbIGATA vs WT (LPM + SPM)
activated
suppressed
Arginine and proline metabolism
DNA replication
Circadian rhythm
Lysosome biogenesis
Chagas disease
Amoebiasis
Autophagy - animal
MAPK signaling pathway
Viral protein interaction with cytokine and cytokine receptor
IL-17 signaling pathway
NF-kappa B signaling pathway
Lipid and atherosclerosis
Rheumatoid arthritis
Cytokine-cytokine receptor interaction
AGE-RAGE signaling pathway in diabetic complications
NOD-like receptor signaling pathway
TNF signaling pathway
Legionellosis
p.adjust
Count
GeneRatio


A
LPS_24h
LPS_8h
EPX_24h
EPX_8h
PC2: 6% variance
PC1: 89% variance
B
EPX_8hrs vs LPS_8hrs
−Log10 P
Log2 fold change
total = 11351 variables
C
EPX_24hrs vs LPS_24hrs
−Log10 P
Log2 fold change
total = 12041 variables
D
Classical macrophage genes
Treatment
Ctrl_8h
EPX_8h
LPS_8h
Ctrl_24h
EPX_24h
LPS_24h
Nos2
Ccl5
Ccl2
Cxcl10
Cxcl11
Irf5
Cd86
Nfkb1
Il1b
Cxcl9
Il6
Tnf
Stat3
E
Alternatively activated macrophage genes
Mrc1
Pparg
Cd163
Stab1
Cd36
Lgals3
Ccl17
Ccl22
Il4ra
Il10
Arg1
Retnla
F
Macrophage/inflammation-related GO BP terms: EPX_vs_LPS
activated
suppressed
cellular response to macrophage colony-stimulating factor stimulus
antifungal innate immune response
response to macrophage colony-stimulating factor
chronic inflammatory response
phagocytosis, recognition
MyD88-dependent toll-like receptor signaling pathway
phagocytosis, engulfment
cellular response to lipopolysaccharide
positive regulation of phagocytosis
phagocytosis
regulation of phagocytosis
response to lipopolysaccharide
myeloid leukocyte activation
positive regulation of cytokine production
regulation of tumor necrosis factor superfamily cytokine production
negative regulation of tumor necrosis factor superfamily cytokine production
positive regulation of inflammatory response
regulation of inflammatory response
negative regulation of inflammatory response
negative regulation of cytokine production
GeneRatio
p.adjust
Count


A
PC2: 7% variance
PC1: 89% variance
IL4_24h
IL4_8h
EPX_24h
EPX_8hr
B
EPX_8hrs vs IL-4_8hrs
−Log10 P
Log2 fold change
total = 12581 variables
C
EPX_24hrs vs IL-4_24hrs
−Log10 P
Log2 fold change
total = 12581 variables
D
Classical macrophage genes
Treatment
Ctrl_8h
EPX_8h
IL4_8h
Ctrl_24h
EPX_24h
IL4_24h
Irf5
Cd86
Nfkb1
Ccl2
Il1b
Tnf
Cxcl10
Cxcl11
Nos2
Ccl5
Stat3
Il6
Cxcl9
E
Alternatively activated macrophage genes
Stab1
Mrc1
Pparg
Cd163
Il4ra
Il10
Ccl22
Arg1
Klf4
Lgals3
Chil3
Retnla
Ccl17
F
Macrophage/inflammation-related GO BP terms: EPX_vs_IL-4
activated
suppressed
negative regulation of acute inflammatory response
negative regulation of innate immune response
activation of innate immune response
antiviral innate immune response
innate immune response-activating signaling pathway
regulation of monocyte differentiation
positive regulation of monocyte differentiation
positive regulation of innate immune response
regulation of innate immune response
positive regulation of cytokine production
regulation of inflammatory response
cellular response to lipopolysaccharide
cellular response to macrophage colony-stimulating factor stimulus
macrophage proliferation
regulation of macrophage derived foam cell differentiation
response to lipopolysaccharide
positive regulation of myeloid leukocyte differentiation
myeloid dendritic cell differentiation
regulation of myeloid leukocyte differentiation
negative regulation of cytokine production involved in inflammatory response
GeneRatio
p.adjust
Count


A
Acod1
Nos2
Il10
Fold Change
Ctrl
LPS+IFNγ
LPS+IFNγ+EPX
B
MHC-II expression
CD86 expression
MFI x 10^3
MFI x 10^4
C
Oxidative phosphorylation
Oligomycin
FCCP
Antimycin A & Rotenone
OCR (pmol/min/1000 cells)
Time (minutes)
D
Basal Respiration
Maximal Respiration
ATP Production
pmol/min/1000 cells
E
TNFα
IL-6
pg/mL
F
CCL22
CCL17
IL-10


A
- i.n. 40µg LPS
- i.n. 10µg EPX
- i.n. 10µg EPX
0
1
2
3 days
BALB/c mice
Resolution of inflammation
B
Lung injury score
0-16
Ctrl
LPS
LPS+EPX
C
Ctrl
LPS
LPS+EPX
D
Singlets
Live CD45+
Neutrophils
SSC
FSC
CD45
Zombie NIR
CD11b
Ly6G
Ly6G -
Siglec-F +, CD11c neg/low
Eos
SSC
CD11c
Monocytes
MerTK- CD11b+
IM
TM
CD11b
MerTK
SSC
Ly6C
Siglec-F
CD11c
Siglec-F - CD11c -
Siglec-F + CD11c +
Polarization
CD206
MHC-II
AM
MerTK
SSC
E
Eosinophils
% Eosinophils (on live CD45+ cells)
Neutrophils
% Neutrophils (on live CD45+ cells)
Inflammatory monocytes
% Inflammatory monocytes (on live CD45+ cells)
Patrolling monocytes
% Patrolling monocytes (on live CD45+ cells)
IM
% IM (on live CD45+ cells)
Classically activated IM
% MHC-II+CD206- (on IM)
Alternatively activated IM
% MHC-II-CD206+ (on IM)
AM
% AM (on live CD45+ cells)
Ctrl
LPS
LPS+EPX

Supplementary Files

This is a list of supplementary files associated with this preprint. Click to download.

- MovieS1CtrlBMDMs.mov
- MovieS4EPXBMDMs.mov
- AlbarracinMeloetal.SupplementaryMaterial.docx
- MovieS3IL4BMDMs.mov
- MovieS2LPSBMDMs.mov
- MovieS5InteractionofEPXwithCD11b.mov